ORIGINAL ARTICLE

Open Access

Topography Modeling of Surface Grinding Based on Random Abrasives and Performance Evaluation

Yanbin Zhang[1], Peng Gong[1], Lizhi Tang[1], Xin Cui[1], Dongzhou Jia[2,3], Teng Gao[1], Yusuf Suleiman Dambatta[1,4] and Changhe Li[1*]

Abstract

The surface morphology and roughness of a workpiece are crucial parameters in grinding processes. Accurate prediction of these parameters is essential for maintaining the workpiece's surface integrity. However, the randomness of abrasive grain shapes and workpiece surface formation behaviors poses significant challenges, and accuracy in current physical mechanism-based predictive models is needed. To address this problem, by using the random plane method and accounting for the random morphology and distribution of abrasive grains, this paper proposes a novel method to model CBN grinding wheels and predict workpiece surface roughness. First, a kinematic model of a single abrasive grain is developed to accurately capture the three-dimensional morphology of the grinding wheel. Next, by formulating an elastic deformation and formation model of the workpiece surface based on Hertz theory, the variation in grinding arc length at different grinding depths is revealed. Subsequently, a predictive model for the surface morphology of the workpiece ground by a single abrasive grain is devised. This model integrates the normal distribution model of abrasive grain size and the spatial distribution model of abrasive grain positions, to elucidate how the circumferential and axial distribution of abrasive grains influences workpiece surface formation. Lastly, by integrating the dynamic effective abrasive grain model, a predictive model for the surface morphology and roughness of the grinding wheel is established. To examine the impact of changing the grit size of the grinding wheel and grinding depth on workpiece surface roughness, and to validate the accuracy of the model, experiments are conducted. Results indicate that the predicted three-dimensional morphology of the grinding wheel and workpiece surfaces closely matches the actual grinding wheel and ground workpiece surfaces, with surface roughness prediction deviations as small as 2.3%.

Keywords Surface topography prediction, Grinding, Grinding wheel model, Random plane method

*Correspondence:
Changhe Li
sy_lichanghe@163.com
Full list of author information is available at the end of the article

Zhang *et al. Chinese Journal of Mechanical Engineering*   (2024) 37:93

Page 2 of 23

1 Introduction

Superalloys are used to manufacture turbine discs and blades for engine hot-end components due to their high strength and oxidation resistance at high temperatures, accounting for more than 50% of the materials used in aircraft engines [1–3]. High-temperature nickel-based alloys (e.g., GH4169, GH4049, etc.) have been developed to meet the demands for high-temperature resistance and stress-bearing capacity [4–6]. However, the low thermal conductivity of GH4169 leads to heat buildup during grinding, causing deterioration in the surface quality of the workpiece [5, 7–9]. To improve surface integrity and achieve green manufacturing, nano-lubricant minimum quantity lubrication (NMQL) has been applied to nickel-based alloy cutting, representing a significant improvement over traditional metal grinding fluids [10–13]. Furthermore, predicting the surface morphology and roughness in nickel-based alloy grinding with NMQL has become a research focus, which is key to advancing aerospace parts manufacturing from green precision methods to intelligent and efficient processes [14–17].

The abrasives on the grinding wheel remove material from the workpiece by cutting. Predicting workpiece surface morphology and roughness remains challenging due to the complex shapes and distribution of abrasives [18–20]. Modeling a single abrasive, as the basic unit on the wheel, is crucial [21–24]. Liu et al. [25] developed a prediction model for workpiece surface roughness using a 3D grinding wheel model (spherical, truncated cone, and cone abrasives) based on a 2D cutting edge profile. Zhang et al. [26] established a 3D morphology and surface roughness prediction model for axial ultrasonic-assisted cross grinding using spherical abrasive modeling. Dong et al. [27] simulated the machining process and predicted the appearance of the finished surface using a mathematical model of the distribution of cone abrasives in the sand belt, accounting for abrasive wear in their study [28]. In the study by Yan et al. [29], the surface morphology of the wheel was measured using a white-light interferometer, and they proposed that abrasives in grinding could be simplified as cones. Hegeman et al. [30] established the 3D surface morphology of the wheel based on ellipsoidal abrasives. Additionally, considering the influence of abrasive position, a random vibration function was added to the ellipsoidal abrasives. Xiao et al. [31] developed a surface morphology model for the specific stacking effect in gear grinding, elucidating the abrasive grain removal mechanism applicable to workpieces with complex geometries. Zhang et al. [32] created a surface morphology model for grinding hard alloys and analyzed the influence of wheel morphology on the maximum material removal rate. Eder et al. [33] investigated the evolution process of surface morphology in nano-grinding

and deduced the governing evolution laws. Kang et al. [34] established a three-dimensional morphology model for circular abrasive grains in slider seat rings, exploring the effect of abrasive grain overlap rate on workpiece morphology and removal rate. Wu et al. [35] developed a surface roughness model for ductile-brittle materials, investigating the effect of brittle fracture on surface morphology and the influence of processing parameters on surface roughness.

Additionally, the spatial distribution of abrasives on the wheel surface significantly affects surface roughness. Scholars have used analytical models based on probability analysis to describe the randomness of the grinding process. Hou and Komanduri [36] found that the particle size of abrasives on the wheel follows a normal distribution [37]. Chen and Rowe [38–40] proposed a method to determine the position of abrasives on the wheel by randomly distributing them based on the spatial position distribution of abrasives [41]. Zhang et al. [42] established an abrasive position model with a normal distribution through the random movement of abrasives in the X, Y, and Z directions during wheel modeling.

However, there are some shortcomings in the existing research on 3D models of the wheel and the surface morphology of the workpiece. Firstly, the modeling of abrasive morphology on the wheel is based on known shape models such as spherical, conical, or hexahedral, which differ from the actual shape of abrasives [43, 44]. Additionally, in the process of modeling workpiece surface morphology, the grinding is based on the geometry of known abrasives, making it inconsistent with the actual workpiece surface morphology [45, 46]. Therefore, establishing a random geometry model for actual abrasives is key to accurately modeling the wheel and workpiece surface morphology [47].

To address the randomness of abrasive shapes and the complexity of material removal in grinding, a single abrasive geometry model based on the random plane method is established. Then, the kinematic model of a single abrasive and the interference geometry model of abrasive/workpiece interaction were established to predict surface morphology [48].

2 Geometric Modeling of Wheel Based on Random Plane

2.1 Random Plane Abrasive Modeling

Both natural and artificial abrasives must undergo crushing to determine particle size. The geometric characteristics and sizes of abrasives after crushing are highly random due to the disordered crushing process. As shown in Figure 1, the morphology of abrasives was observed using laser confocal microscopy. During abrasive crushing, internal defects in the material cause dislocation and slip between
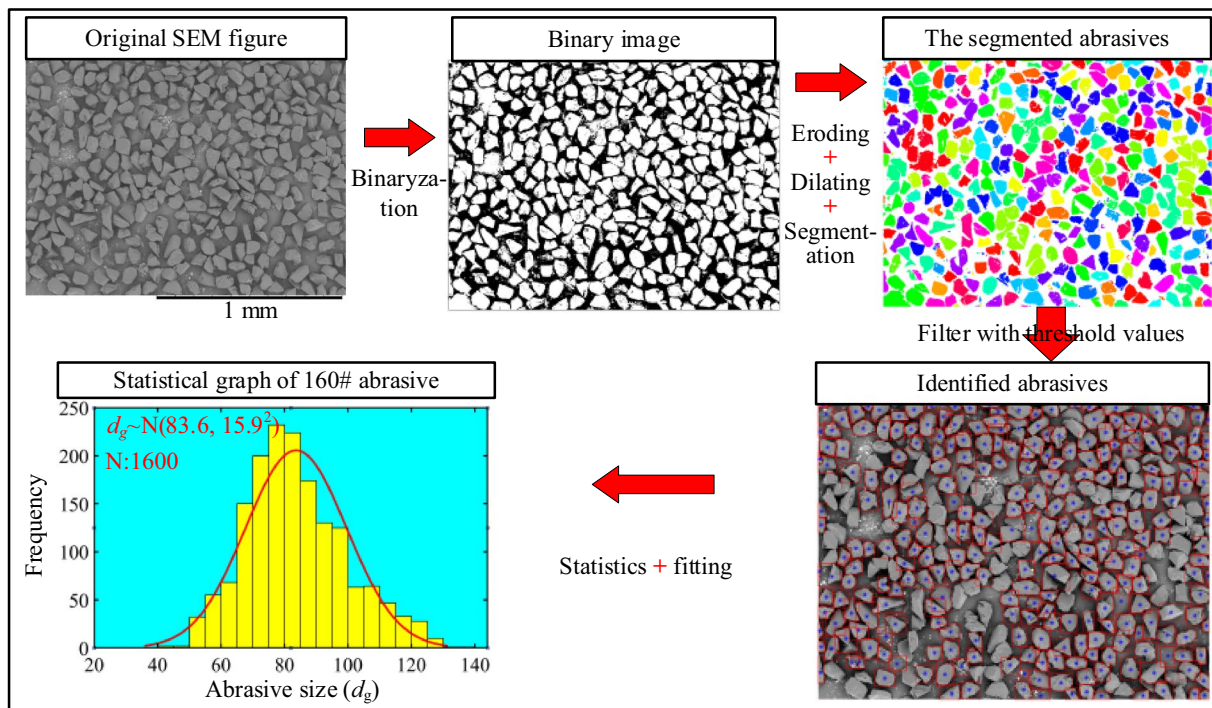
Figure 1 Abrasive morphology and binary image

internal grains under external pressure, resulting in brittle fracture [49–52]. Therefore, the abrasives have the following characteristics: they are irregular polyhedra with a random number of faces. The size of the abrasives varies randomly within a certain range, and the mesh number of the wheel characterizes the particle size of the abrasives.

A random plane abrasive modeling method is proposed: multiple random planes are established, and the shape enclosed by these planes is defined as the surface of random abrasives. The specific method is as follows:

First, a spherical equation limiting the minimum particle size of abrasives is established with the origin of coordinates as the center:

$$x^2 + y^2 + z^2 = r^2. \tag{1}$$

Random points on the sphere are randomly selected as the base point to establish the section plane of the sphere (that is, a random plane). The coordinates of random points conform to the following equation:

$$\begin{cases} x_i = \pm r \cdot rand, \\ y_j = \pm r \cdot rand, \\ x_i^2 + y_j^2 + z_k^2 = r^2. \end{cases} \tag{2}$$

Then a plane tangent to the sphere is established by random points (x_i, y_j, z_k) on the sphere. The equation of the tangent plane is as follows:

$$x_i x + y_j y + z_k z = r^2. \tag{3}$$

A single abrasive is formed by establishing multiple random planes, as shown in Figure 2. Processing the obtained MATLAB random planar graph data. A closed 3D abrasive shape can be obtained by removing the excess between the intersecting planes and selecting the minimum volume figure under multiple plane equations [53].

For a given mesh number of wheels, the particle size varies within a certain range [D_{min}, D_{max}] and follows a normal distribution. Therefore, the side length of the cuboid domain generated by abrasives is set to D_{max} to limit the maximum particle size, and the sphere diameter is set to D_{min} to limit the minimum particle size. When the initial number of planes is set to 30 or 70, the resulting abrasive grains do not match those scanned by SEM (as shown in Figure 2). Through measurement of actual abrasives, it was found that when the initial number of planes is 40 to 50, the abrasive morphology is closest to the real morphology.

2.2 Random Distribution of Abrasives and Modeling of Wheel

A portion of the area involved in grinding on the wheel was selected for modeling, as shown in
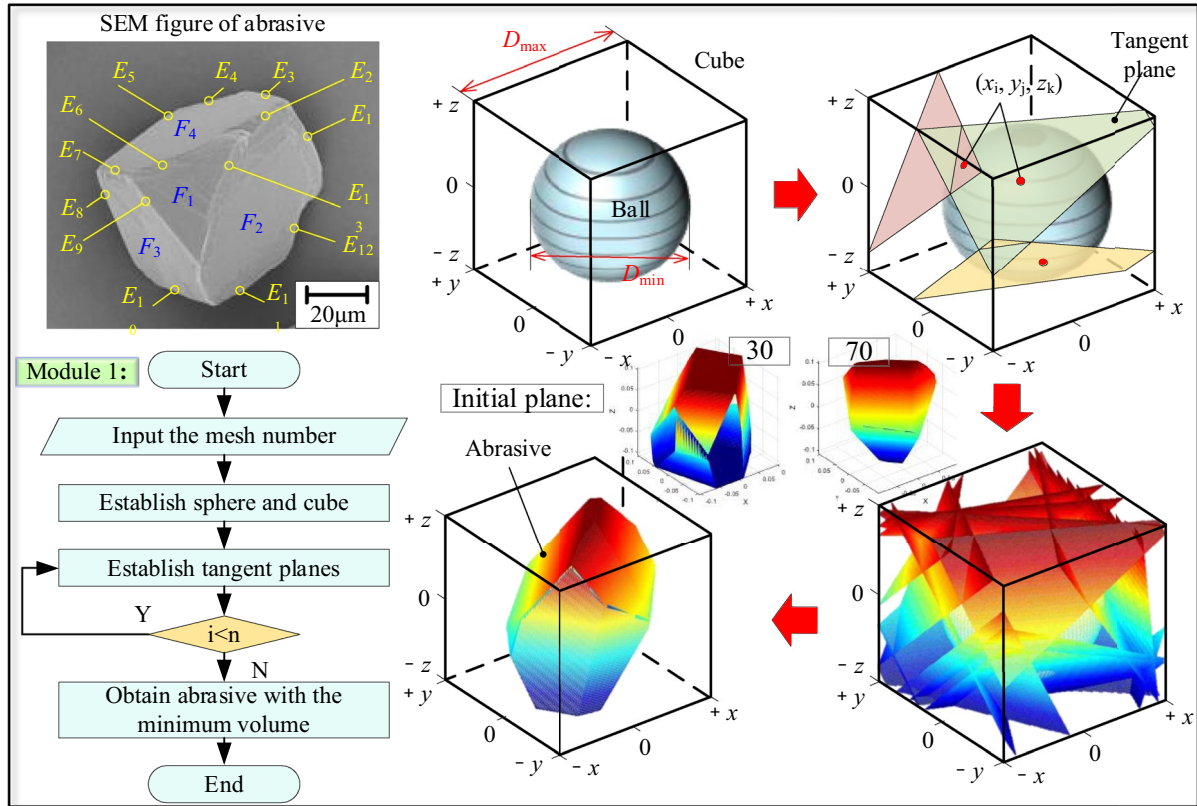
Figure 2 Stochastic abrasive modeling method

Figure 3(a). The sampling width and length of the wheel are denoted as W and L, respectively. Since abrasive grains are randomly distributed on the grinding wheel surface, the grain size distribution is determined by randomly selecting the sampling range. To facilitate the analysis of abrasive grain morphology, half of the sampling length is chosen to be equal to the sampling width.

Hou and Komanduri [36] found that the abrasives on the wheel obey the normal distribution, and according to the 3σ principle of the normal distribution, it can be expressed as:

$$\Phi(d_g) = \frac{1}{\sqrt{2\pi}\sigma} \exp\left[-\frac{(d_g - D_{ave})}{2\sigma^2}\right], \quad (4)$$

where d_g is the abrasive diameter, σ is the standard deviation of abrasive diameter, and D_{ave} is the mean abrasive diameter.

The wheel is composed of abrasive, binder, and porosity. The volume fraction of abrasive can be calculated by the wheel tissue number S. Thus, the abrasive spacing can be obtained:

$$L_r = D_{ave}\left(\sqrt{\frac{\pi}{8(32-S)}} - 1\right). \quad (5)$$

Therefore, the number of abrasives in the axial and circumferential direction of the wheel is:

$$N_x = \frac{L}{D_{ave}+L_r}, \quad (6)$$

$$N_y = \frac{W}{D_{ave}+L_r}. \quad (7)$$

The surface of the wheel is dispersed into several small cuboids, as shown in Figure 3(b) The initial coordinates of the abrasive are in the center of the small cube, and the side length of the cube is $D_{ave}+L_r$.

Further, the position of abrasives is arranged on the surface of the wheel according to the distance between abrasives. A randomly transformed position coordinate is applied to each abrasive to realize the random distribution of abrasive positions in axial, circumferential and protruding heights. The central position coordinate matrix of abrasives is as follows:
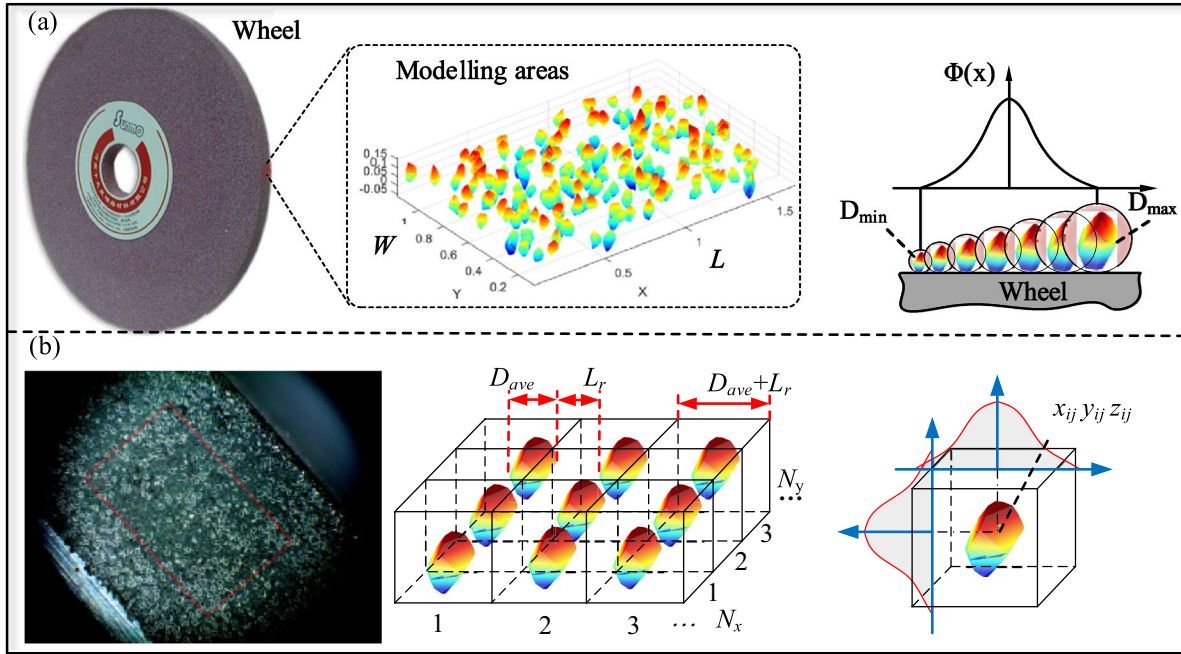
Figure 3 Wheel modeling area and schematic diagram of abrasive position: (**a**) modeling of local abrasive grains on the grinding wheel surface, (**b**) distribution of abrasive grain morphology in the grinding wheel model)

$$\left(x_{ij}', y_{ij}', z_{ij}'\right)^{\mathrm{T}} = \left(j \cdot L_g \cdot i \cdot L_g \cdot 0\right)^{\mathrm{T}}, \ 1 \leq i \leq N_x, 1 \leq i \leq N_y, \tag{8}$$

where x_{ij}', y_{ij}', and z_{ij}' are the initial coordinates of the abrasives in row i and column j, $L_g = L_r + D_{ave}$.

Further, the position of the abrasives is randomly transformed, and the transformed coordinates are:

$$\left(x_{ij}, y_{ij}, z_{ij}\right)^{\mathrm{T}} = \left(x_{ij}' + \Delta x_{ij}, y_{ij}' + \Delta y_{ij}, z_{ij}' + \Delta z_{ij}\right)^{\mathrm{T}}, \tag{9}$$

where x_{ij}, y_{ij}, and z_{ij} are the position coordinates of the corresponding abrasive after random transformation. Δx_{ij}, Δy_{ij}, and Δz_{ij} are the coordinate values transformed by each abrasive in three directions, respectively, and their sizes are set according to the method studied by Zhang et al. [54, 55].

In addition, to ensure that the positions of abrasives will not overlap and collide after random movement, the motion relationship between abrasives should also meet the following requirements:

$$\sqrt{\left(x_{ij} - x_{i++j++}\right)^2 + \left(y_{ij} - y_{i++j++}\right)^2} \geq \frac{D_{ij} + D_{i++j++}}{2}. \tag{10}$$

The calculation process and results of the geometric model of the wheel are illustrated in Figure 4. For the resin-based bonded corundum wheel (outer diameter 300 mm, inner diameter 76.2 mm, thickness 20 mm), the sampling area of the wheel is a rectangle with dimensions 1 mm width and 2 mm length [56]. The 3D morphology of the sampled area of the wheel with different grit sizes (80#, 160#, and 240#) is depicted.

The 3D morphology of the simulated wheel was validated, as shown in Figure 5. The actual wheel profile can be used to analyze the prominent positions and distances of abrasives [57]. The distances and height differences of abrasive vertices can be analyzed, and the simulation results agree well with the experimental values. The effective height difference of the wheel surface is 300 μm, consistent with the height difference of the abrasives on the simulated wheel surface. Furthermore, the contour height curves of the wheel surface closely match the calculated positional characteristics of the abrasives.

3 Workpiece Surface Morphology Generative Model

3.1 Contact Arc Length of a Single Abrasive Cutting Workpiece

The coordinate system is established with the lowest point of contact between the wheel and the workpiece as the origin of the grinding process. The X, Y, and Z axes correspond to the coordinate system of the grinding machine,
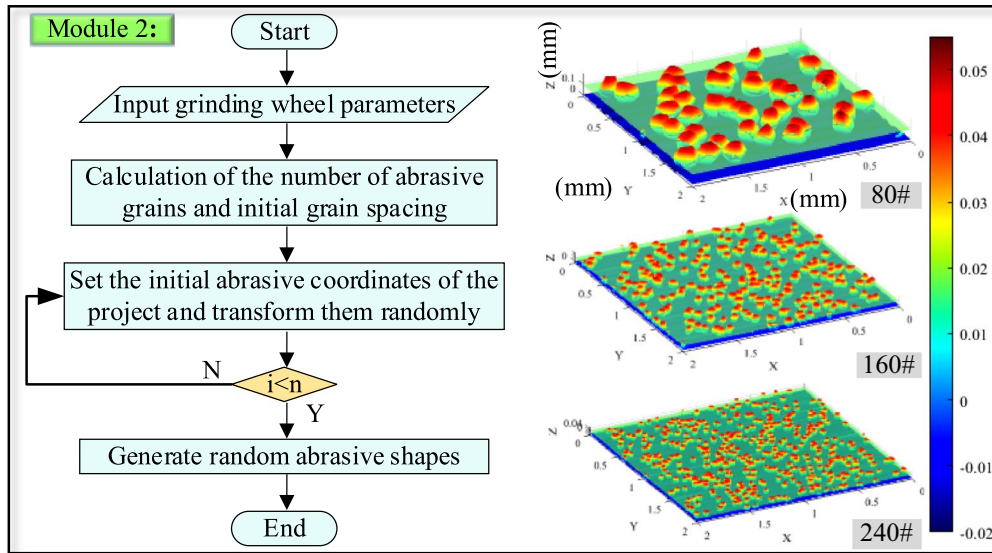
Zhang *et al. Chinese Journal of Mechanical Engineering*   (2024) 37:93

Page 6 of 23

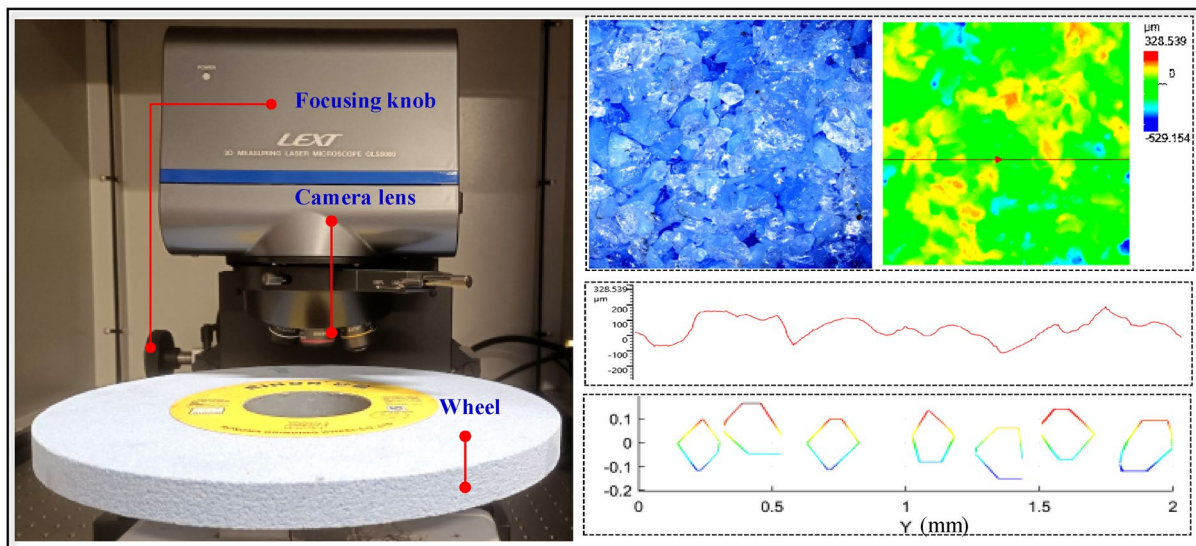**Figure 4** Grinding wheel morphology calculation process

Figure 5 The simulation and experimental results

respectively. The motion diagram of a single abrasive is depicted in Figure 6.

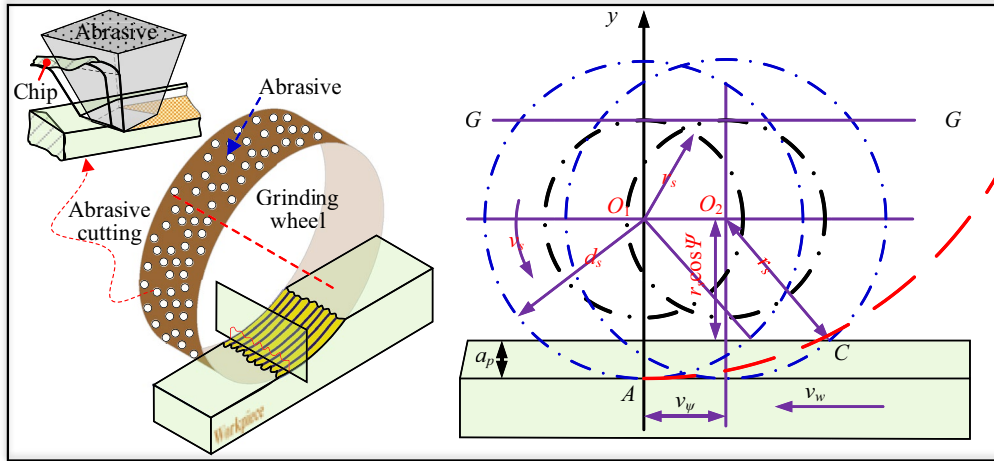The contact arc length between a single abrasive and the workpiece is *AC*, and according to the relative motion relationship between the wheel and the workpiece, the equation of the cycloid is:

$$\begin{cases} x = r_s \sin \psi \pm v_\psi, \\ y = r_s(1 - \cos \psi), \end{cases} \tag{11}$$

where Ψ is the angular displacement of the abrasive, v_Ψ is the horizontal movement distance of the wheel, "+" represents reverse grinding, "−" represents smooth grinding.

$$v_\psi = \frac{\psi \cdot v_0}{2\pi}, \tag{12}$$

where v_0 is the horizontal movement distance of the workpiece corresponding to each rotation of the wheel, and its expression is:

Figure 6 Single abrasive trajectory and contact arc length

$$v_\psi = \frac{\psi \cdot v_0}{2\pi} = \frac{v_w}{60n_s \times 2\pi}\psi = \frac{v_w}{60n_s \times 2\pi}\frac{r_s}{r_s}\psi = \frac{r_s v_w}{60v_s}\psi,$$

(13)

where, n_s represents the rotational speed, v_w denotes the workpiece feed rate, r_s signifies the grinding wheel radius, and v_s indicates the peripheral speed of the grinding wheel.

Plug v_Ψ in the cycloidal equation:

$$\begin{cases} x = r_s\left(\sin\psi \pm \dfrac{v_w}{60v_s}\psi\right), \\ y = r_s(1 - \cos\psi). \end{cases}$$

(14)

Differentiate the above equation:

$$\begin{cases} \mathrm{d}x = r_s\left(\cos\psi \pm \dfrac{v_w}{60v_s}\right)\mathrm{d}\psi, \\ \mathrm{d}y = r_s\sin\psi\, d\psi. \end{cases}$$

(15)

The differential value of motion contact arc length l_k is:

$$\mathrm{d}l_k = \sqrt{\mathrm{d}x^2 + \mathrm{d}y^2} = \left[r_s^2\left(\cos\psi \pm \frac{v_w}{60v_s}\right)^2 + r_s^2\sin\psi^2\right]^{\frac{1}{2}}\mathrm{d}\psi$$
$$= r_s\left[1 \pm \frac{2v_w}{60v_s}\cos\psi + \left(\frac{v_w}{60v_s}\right)^2\right]^{\frac{1}{2}}\mathrm{d}\psi.$$

(16)

Since the value of a_p is very small, Ψ is very small, so $\cos\Psi = 1$. The above equation can be rewritten as:

$$\mathrm{d}l_k = r_s\left[1 \pm \frac{2v_w}{60v_s} + \left(\frac{v_w}{60v_s}\right)^2\right]^{\frac{1}{2}}\mathrm{d}\psi$$
$$= r_s\left(1 \pm \frac{v_w}{60v_s}\right)\mathrm{d}\psi.$$

(17)

Integrate the above equation:

$$l_k = r_s\left(1 \pm \frac{v_w}{60v_s}\right)\int_0^\psi \mathrm{d}\psi = r_s\left(1 \pm \frac{v_w}{60v_s}\right)\psi.$$ (18)

Due to the value of Ψ is small, so $\sin\Psi = \Psi$, then:

$$\psi = \sqrt{1 - \cos^2\psi} = \left[1 - \left(\frac{r_s - a_p}{r_s}\right)^2\right]^{\frac{1}{2}}$$
$$= 2\left[\frac{a_p}{d_s} - \frac{a_p^2}{d_s^2}\right]^{\frac{1}{2}} \approx 2\sqrt{\frac{a_p}{d_s}},$$

(19)

where, d_s represents the radius of the grinding wheel post-grinding.

Then the value of Ψ is substituted into the arc length equation (18):
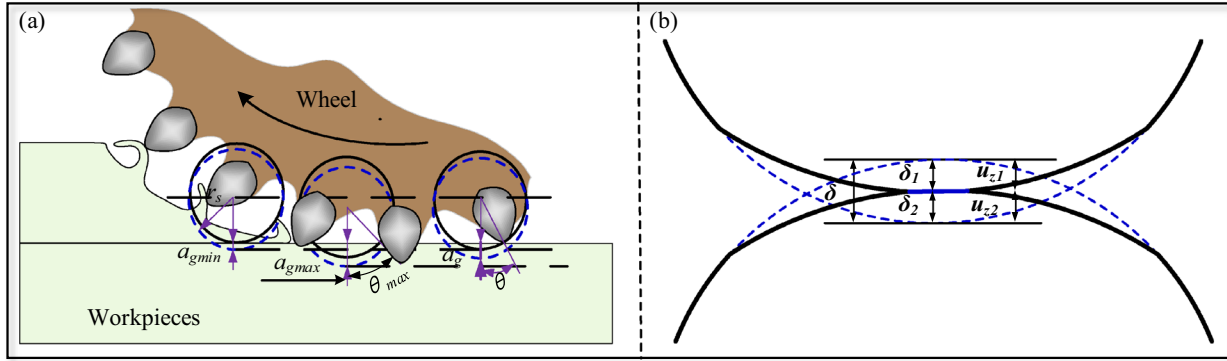
Figure 7 Schematic diagram of elastic deformation of workpiece surface and elastic sphere geometric contact: (**a**) actual elastic recovery amount, (**b**) schematic diagram of geometric contact with elastic balls

$$l_k = 2r_s \left(1 \pm \frac{v_w}{60v_s}\right)\sqrt{\frac{a_p}{d_s}} = \left(1 \pm \frac{v_w}{60v_s}\right)\sqrt{a_p \cdot d_s}. \tag{20}$$

Further, according to Eq. (11), the motion equation of abrasives can be derived and expressed as:

$$y = \frac{x^2}{d_s\left(1 \pm \frac{v_w}{v_s}\right)^2}. \tag{21}$$

3.2 Furrow Depth of a Single Abrasive Cutting Workpiece

The actual cutting depth is less than the theoretical value due to material recovery after elastic deformation during grinding [58]. Therefore, the actual surface curve of the workpiece should account for the elastic recovery, as depicted in Figure 7(a).

Taking the surface of the workpiece after machining as the reference plane, the cutting depth equation of the abrasive can be expressed as:

$$h = a_p - \frac{x^2}{d_s\left(1 \pm \frac{v_w}{v_s}\right)^2}. \tag{22}$$

The height of actual workpiece surface formed during the grinding of a single abrasive is:

$$Z_n = z_n + \varepsilon_{wn}, \tag{23}$$

where Z_n is the actual coordinate height value of the workpiece, z_n is the theoretical coordinate height value of the workpiece. ε_{wn} is the elastic recovery amount of the workpiece can be solved according to Hertz contact theory. The schematic diagram of elastic sphere geometric contact is illustrated in Figure 7(b).

When two elastic spheres come into contact with different radii, the pressure of the two spheres at r distance from the center point is:

$$p(r) = p_0\sqrt{1 - \left(\frac{r}{a}\right)^2}, \tag{24}$$

where p_0 is the maximum pressure in the contact area of the two spheres and a is the radius of the contact surface.

The displacements are determined at distances r from the center of the sphere within the contact circle, as well as at points outside the contact circle at various distances r from the center.

$$\begin{cases} u_z(r) = \dfrac{1-v^2}{E} \dfrac{\pi \cdot p_0}{4a}\left(2a^2 - r^2\right), r \leq a, \\[3mm] u_z(r) = \dfrac{1-v^2}{E} \dfrac{p_0}{2a}\left[\left(2a^2 - r^2\right)\sin^{-1}\left(\dfrac{a}{r}\right) + a \cdot r \cdot \sqrt{a - \left(\dfrac{a}{r}\right)^2}\right], r > a, \end{cases} \tag{25}$$

where v and E are the Poisson's ratio and elastic modulus of the workpiece respectively.

Due to the action of pressure, the elastic deformation of the two spheres occurs at the contact point, the displacement in the contact area is:

$$u(r) = u_{z1} + u_{z2} = \delta - \frac{r^2}{2R^*}, \tag{26}$$

where δ is the deformation of the two elastic spheres and R^* is the comprehensive radius of curvature of the two spheres.

$$\frac{1}{R^*} = \frac{1}{R_1} + \frac{1}{R_2}. \tag{27}$$

Since each point on the contact surface has the same pressure value in the two elastic spheres, then:

$$\begin{aligned} u(r) = u_{z1} + u_{z2} &= \frac{1 - v_1^2}{E_1}\frac{\pi \cdot p_0}{4a}\left(2a^2 - r^2\right) + \frac{1 - v_2^2}{E_2}\frac{\pi \cdot p_0}{4a}\left(2a^2 - r^2\right) \\ &= \frac{1}{E^*}\frac{\pi \cdot p_0}{4a}\left(2a^2 - r^2\right). \end{aligned} \tag{28}$$

By combining Eqs. (26) and (28), it can be got:

$$\frac{\pi \cdot p_0}{4aE^*}\left(2a^2 - r^2\right) = \delta - \frac{r^2}{2R^*}. \tag{29}$$

When $r = a$, the radius of the contact circle can be found as:

$$a = \frac{\pi \cdot p_0 \cdot R^*}{2E^*}. \tag{30}$$

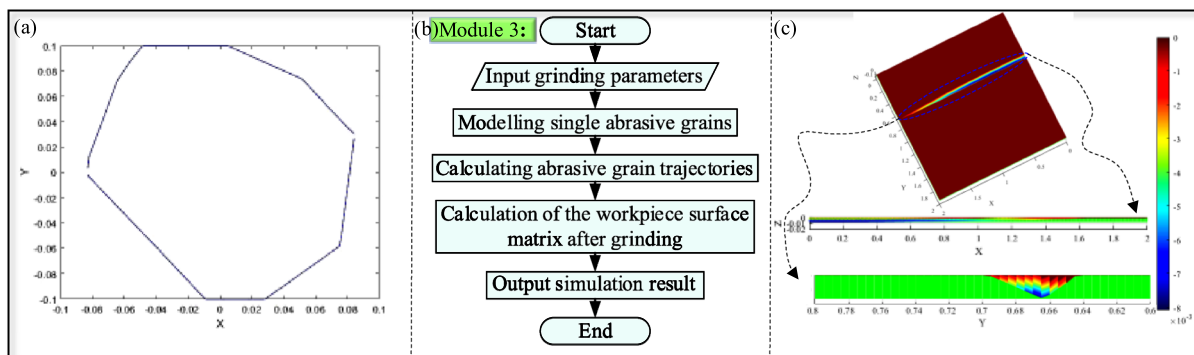Therefore, the sum of the deformations of two elastic spheres can be found when $r = 0$:

$$\delta = \frac{\pi \cdot a \cdot p_0}{2E^*}. \tag{31}$$

According to Hertz contact theory, the contact model between the abrasive and the workpiece during grinding can be described as contact between a rigid abrasive and an elastic workpiece. When solving this model, the curvature radius R of the contact point between the abrasive and the workpiece is considered, where the workpiece is treated as having an infinite radius and the abrasive as infinitely stiff relative to the workpiece.

$$\frac{1}{R^*} = \frac{1}{R_1} + \frac{1}{R_2} = \frac{1}{R} + 0 = \frac{1}{R}. \tag{32}$$

Then $R^* = R$.

$$\frac{1}{E^*} = \frac{1 + v_1^2}{E_1} + \frac{1 + v_2^2}{E_2} = 0 + \frac{1 + v^2}{E} = \frac{1 + v^2}{E}. \tag{33}$$

Figure 8 Calculation process in workpiece grinding with single abrasive: (**a**) maximum cross-sectional profile curve, (**b**) surface profile of individual abrasive grain randomly generated, (**c**) surface morphology diagram of individual abrasive grain grinding workpiece

Table 1 Grinding parameters

Grinding parameters	Number
Grinding wheel diameter d_s	300 mm
Grain size	80
Peripheral speed of the grinding wheel v_s	30 m/s
Workpiece feed rate v_w	0.05 m/s
Grinding depth a_p	20 μm
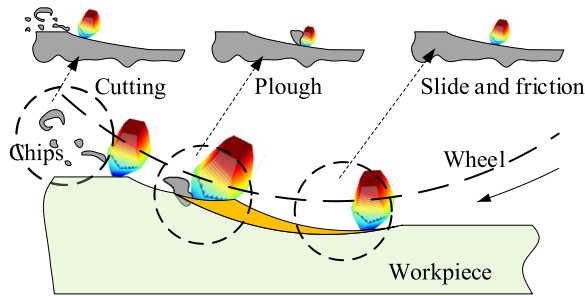
Figure 9 Mechanism of multi-abrasive grinding

Substitute the above equation into Eqs. (30) and (31) to obtain the contact circle radius and elastic deformation of the workpiece ε_{wn} of the contact area between the abrasive and the workpiece surface and:

$$a = \sqrt[3]{\frac{3P}{4} \cdot \frac{R \cdot (1+v^2)}{E}}, \tag{34}$$

$$\varepsilon_{wn} = \frac{a^2}{R} = \sqrt[3]{\frac{9P^2}{16R\left(\frac{1+v^2}{E}\right)^2}}. \tag{35}$$

3.3 Modelling of Single Abrasive Cutting Furrow Morphology

When calculating the material removal of a single abrasive during grinding, it is necessary to determine the interference area between the abrasive and the workpiece. This involves the maximum cross-section profile curve of random abrasives engaged in cutting during grinding, as depicted in Figure 8(a).

Before calculating the grinding of a single abrasive, the coordinate matrix of the upper surface of the workpiece is defined first, and let the $z=0$ plane as the initial surface of the workpiece. Then the workpiece surface matrix is:

$$\mathbf{Z} = \begin{bmatrix} z_{11} & z_{12} & \cdots & z_{1n} \\ z_{21} & z_{22} & \cdots & z_{2n} \\ \vdots & \vdots & \ddots & \vdots \\ z_{m1} & z_{m2} & \cdots & z_{mn} \end{bmatrix}, \tag{36}$$

where m and n are respectively the number of points after discretizing the workpiece in x and y direction.

Initially, the size range of abrasives and the maximum and minimum particle sizes are determined, and the random surface morphology of a single abrasive is generated, as shown in Figure 8(b). The profile matrix of a single abrasive in the YOZ plane was extracted, and the workpiece surface matrix after grinding was calculated by integrating the kinematic model of a single abrasive. Finally, the workpiece surface matrix and 3D image were generated.

The grinding parameters are shown in Table 1. The image resulting from grinding the workpiece with a single abrasive is depicted in Figure 8(c). The trajectory generated by a single abrasive on the workpiece surface forms a cycloid. Under the condition of a grinding depth set to 20 μm, numerical analysis shows that the lowest point of the workpiece surface is 16 μm. Due to the elastic deformation of the wheel and the workpiece, as well as variations in particle size, the actual cutting depth is less than the set depth.
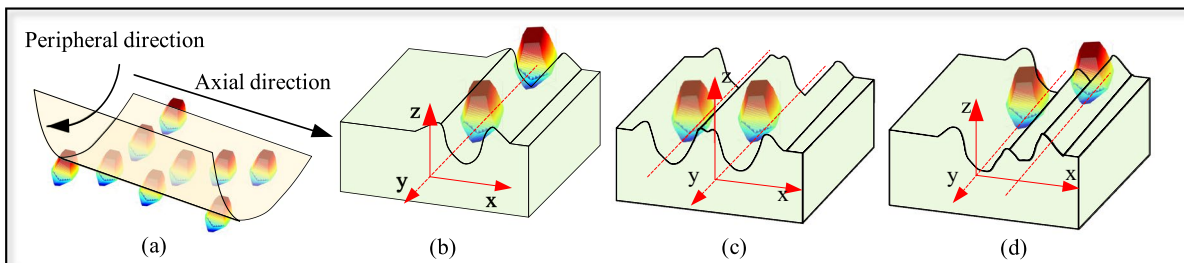
Figure 10 Axial distribution of abrasive particles and grinding mechanism
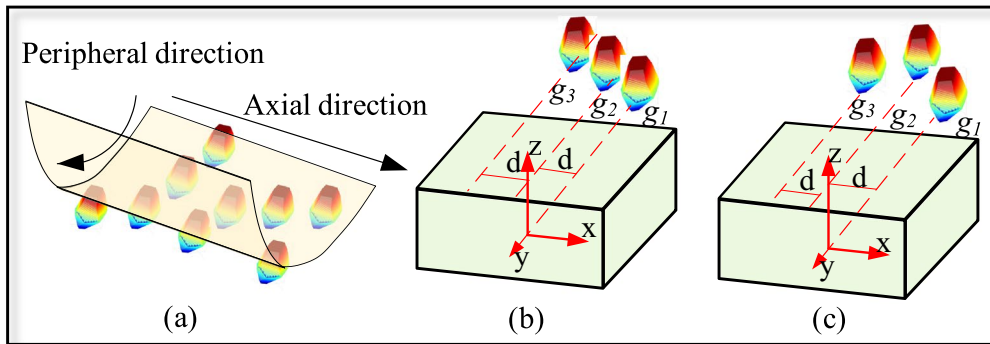
Figure 11 Circumferential distribution of abrasive particles and grinding mechanism

3.4 Modeling the Workpiece Surface in Grinding

During grinding, a series of random interference interactions occur between numerous abrasives and the workpiece surface, shaping the workpiece surface morphology through the collective effects of multiple abrasives [59–63]. The grinding mechanism involving multiple abrasives is depicted in Figure 9. The positioning of abrasives on the wheel also influences the formation of the workpiece surface morphology, a topic analyzed from two perspectives.
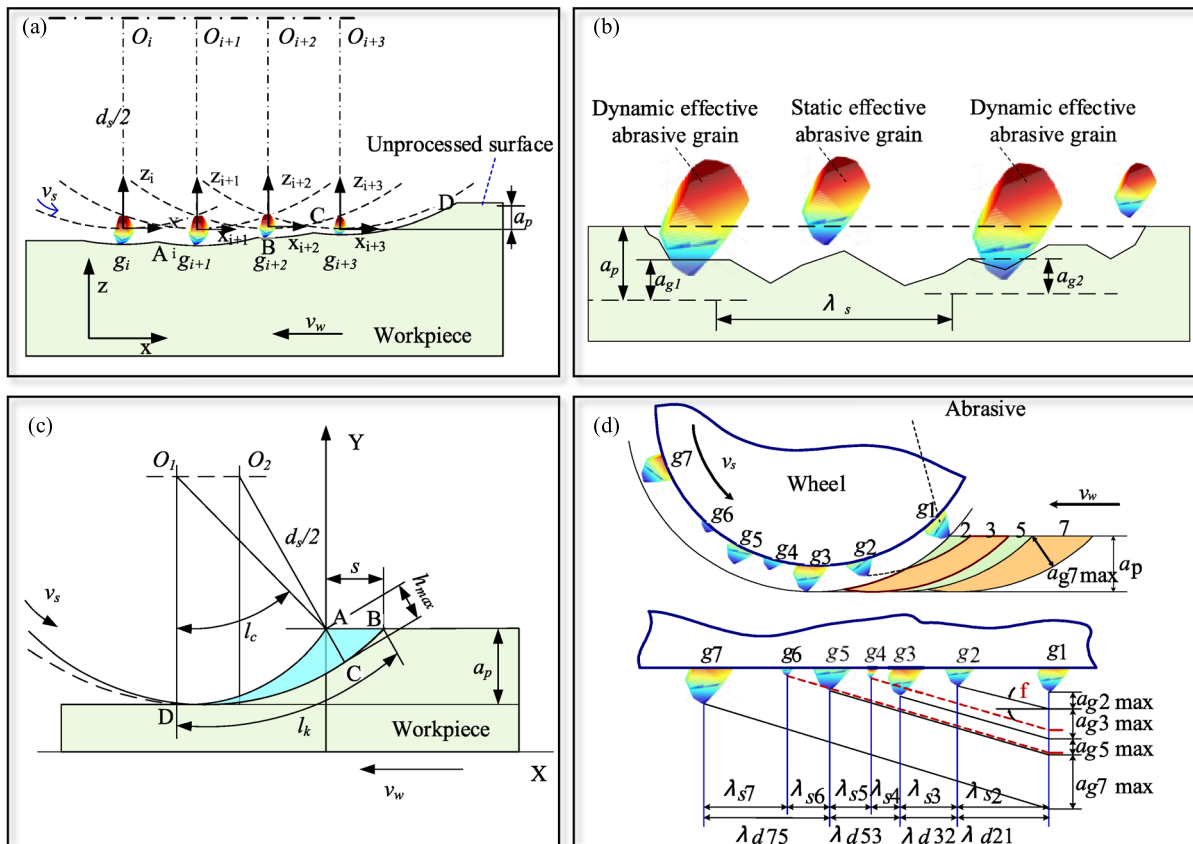
Figure 12 Dynamic effective grain grinding mechanism: (**a**) mechanism of multi-abrasive grinding, (**b**) static effective abrasive, (**c**) maximum undeformed chip thickness, (**d**) dynamic effective abrasive [45]

3.4.1 Influence of the Axial Distribution Mode of Abrasives

The axial distribution position of abrasives and the grinding mechanism were shown in Figure 10(a). When the axial distribution mode of adjacent abrasives is shown in Figure 10(b), the axial position of abrasives overlaps, resulting in furrow overlap on the workpiece surface. When the distribution mode of abrasives is shown in Figure 10(c), the scratch distance generated by abrasive particles is $d_{\max}$, and the furrow distance generated by adjacent abrasives on the workpiece surface is large [64]. When the distribution mode is shown in Figure 10(d), the distance of abrasives is between the first and the second case. Moreover, the movement trajectory between the adjacent two abrasives partially interferes, and the scratch distance generated by abrasives on the workpiece is $0 < d < d_{\max}$.

$$d_{\max} = \frac{2d_g}{\sqrt[3]{v_g}}. \tag{37}$$

3.4.2 Influence of Circumferential Distribution of Abrasives

The difference in the circumferential distance of adjacent abrasives on the wheel results in varying grinding orders on the workpiece. According to the circumferential distribution mode among any three adjacent abrasives on the wheel, the furrow order generated by different abrasives on the workpiece surface varies. The circumferential distribution position of abrasives and the grinding mechanism is shown in Figure 11(a). The sequence of scratches on the surface of the workpiece results from the different order of scratches produced by adjacent abrasives, as shown in Figure 11(b) and (c).

3.4.3 Dynamic Effective Abrasive and Cutting Depth

Considering the kinematic relationship between adjacent abrasives, it is assumed that when the second abrasive inserts into the workpiece, the material is removed completely after the interference between the first abrasive and the workpiece. The motion relationship of adjacent abrasives is depicted in Figure 12(a). When the abrasives remove the material on the surface of the workpiece during movement, the generated Z coordinate falls below 0.

The trajectory of abrasives in the global coordinate system is represented by a function that defines the set of motion trajectories of abrasives. The area of interference between abrasive and workpiece is defined as the maximum contour of each abrasive in the direction perpendicular to the XOZ plane. This contour is discretized into a matrix of points in MATLAB. Therefore, the motion trajectory of abrasives is considered as the collection of points and motion trajectories along the abrasive contour. Due to the random distribution of the abrasive protrusion height, abrasives below the surface of the wheel will not participate in cutting. The abrasives that do participate in cutting are termed dynamic effective abrasives (as shown in Figure 12(b)).

The maximum undeformed chip thickness of two adjacent single abrasives involved in grinding is:

$$h_{\max} = 2 \cdot \lambda \cdot \frac{v_w}{v_s} \cdot \sqrt{\frac{a_p}{D}}. \tag{38}$$

The maximum undeformed chip thickness of abrasive is shown in Figure 12(c), $h_{\max}$ is the maximum undeformed chip thickness [65, 66]. The cutting depth of abrasive increases to $h_{\max}$ first and then decreases gradually. λ is the spacing of abrasives for continuous cutting. According to Eq. (19), $2\sqrt{\frac{v_w}{v_s}}$ represents the angular displacement ψ of the abrasive grain, and $\frac{v_w}{v_s}$ denotes the grinding depth, where the maximum undeformed chip thickness is directly influenced by the grinding depth.

Wherein, the abrasive spacing and the protruding height of each abrasive on the wheel with orderly arrangement of abrasive are fixed values, while the abrasive distribution position and height are not the same on the disordered wheel. Therefore, when the effective abrasive spacing is λ, the maximum undeformed chip thickness of the abrasive grain is:

$$h_{\max(n)} = 2 \cdot \lambda_{(n \sim n-1)} \cdot \frac{v_w}{v_s} \cdot \sqrt{\frac{a_p}{D}} + \left(a_{p(n)} - a_{p(n-1)}\right), \tag{39}$$

where $h_{(n)\max}$ is the maximum undeformed chip thickness of the nth dynamic effective abrasive; $\lambda_{(n \sim n-1)}$ is the distance between the nth and $(n-1)_{\text{th}}$ dynamic effective abrasives. $a_{p(n)}$ is the height of the n_{th} dynamic effective abrasive (as shown in Figure 12(d)), and $a_{p(n-1)}$ is the height of the $(n-1)_{\text{th}}$ dynamic effective abrasive.

3.4.4 Modeling Process for Creating Surface Topography

Firstly, the grinding parameters are determined. Then the surface morphology of the wheel is established according to the random single abrasive geometry model and position model. Next, calculate the movement track of each abrasive on the wheel and the scratches formed after interference with the workpiece surface. Finally, the workpiece surface height matrix formed by the interference of all scratches after grinding is computed and subsequently output as images.

The calculation flow of workpiece surface morphology is illustrated in Figure 13. The wheel parameters include the dimensions, the organization, the size, the shape of
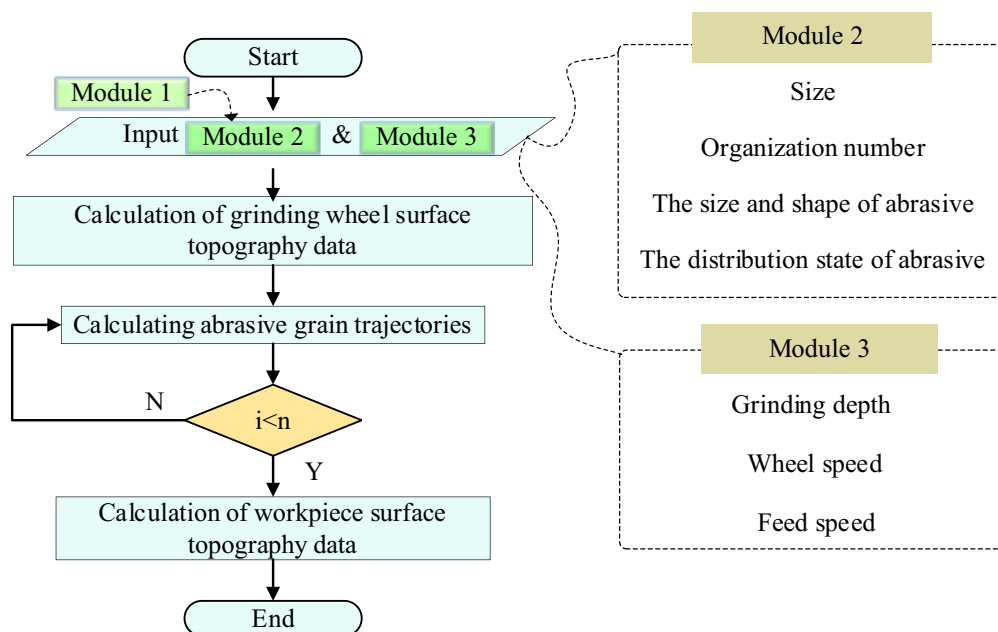
Figure 13 Workpiece surface morphology calculation process

the abrasive, and the distribution state of the abrasive. Machining parameters include grinding depth, wheel speed, and feed speed. Therefore, the calculation results under the comprehensive consideration of many factors are expected to be consistent with real grinding to a certain extent.

4 Experimental Verification and Discussion
4.1 Experimental Setup
4.1.1 Experimental Equipment
This research was conducted using a surface CNC precision grinding machine (K-P36) with a maximum wheel speed of 2000 r/min and a maximum wheel peripheral speed of 50 m/s. (The detailed experimental instruments are shown in Table 2). The wheel used in the experiment was a white corundum wheel with an outer diameter of 300 mm, an inner diameter of 76.2 mm, and a width of 20 mm. The atomization parameters of the micro-lubrication supply equipment can be adjusted by the

frequency generator, the compressed air flow knob, and the flow knob, as shown in Figure 14.

4.1.2 Experimental Material
The experimental material is high temperature nickel-based alloy GH4169, whose chemical composition and mechanical properties are shown in Tables 3 and 4.

In the experiment, soybean oil served as the base oil, and Al_2O_3 nanoparticles were used as the additive phase to prepare a nanofluid with a volume fraction of 2%. Sodium dialkyl sulfate dispersant was added to enhance the dispersion of the nano-lubricant. The nano-lubricant was stirred using an ultrasonic oscillator for 30 minutes. The physical properties of Al_2O_3 nanoparticles are shown in Table 5.

4.1.3 Experimental Scheme
The lubrication condition used in the experiment is NMQL, and the single factor variable method is

Table 2 Description of the instruments and machines parameters

Experimental instruments	Manufacturer	Applications
Scanning electron microscope (SEM)	CARL ZEISS	Figure 1
Olympus 3D Measurement Laser Confocal Microscope OLS5000	Jiangsu Jians (Suzhou) Intelligent Technology Co., Ltd.	Figure 5
Grinding machine K-P36	SCHLEIFRING Machinery (Shanghai) Co.	Figure 14
KS-2106 Micro Lubrication Device	Shanghai Jinzhao Energy Technology Co., Ltd. (CN)	Figure 14
Ultrasonic oscillator	Shenzhen Jiemeng Cleaning Equipment Co.	Table 5
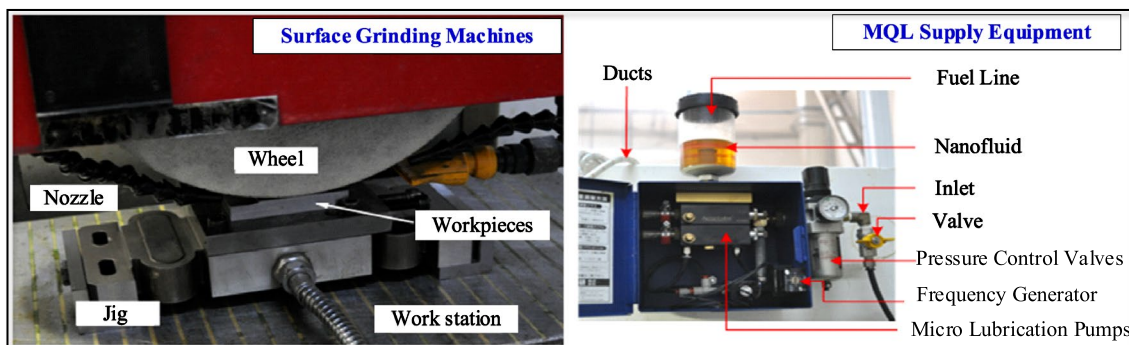
Figure 14 Grinding experimental equipment

employed to investigate the influence of different mesh sizes of wheels and varying grinding depths on the surface morphology of the workpiece. The experimental scheme is shown in Table 6. After the experiment, the workpiece surface was cleaned with anhydrous ethanol and dried by blowing. The 3D morphology of the workpiece was scanned using a laser confocal microscope, and the surface roughness value was calculated for different grinding parameters.

4.2 Influence of Wheel Mesh on Workpiece Morphology
4.2.1 Prediction Result
The 3D morphology of the workpiece was observed under different mesh sizes (80#, 160#, and 240 #) with a grinding depth ap of 20 μm, as shown in Figure 15. With the increase in wheel mesh size, the number of abrasives on the wheel increases and the spacing between abrasives decreases. The number of grinding marks produced on the workpiece surface increases. Additionally, with the increase in the number of abrasives, the interference between scratches produced by different abrasives also increases, thereby contributing to the formation of a better surface morphology of the workpiece [67, 68]. As the mesh size increases, the height difference between the peaks and troughs of the workpiece contour curve increases, and the distance between adjacent peaks and troughs in the *X*-axis direction decreases significantly.

Based on the 3D morphology of the workpiece, the surface contour curve is generated by extracting the height matrix from a specific section. The roughness value of the workpiece surface at this point is calculated [69]. Further, the roughness values of different positions on the workpiece are calculated multiple times, and their average value is obtained. The corresponding relationship between the mesh size of wheels and the surface roughness of the workpiece is determined. As the mesh size increases, the surface quality improves, and the roughness value *Ra* decreases from 3.39 μm to 1.17 μm.

4.2.2 Experimental Result
The surface morphology and roughness profile curves of the workpiece after grinding with different mesh sizes are illustrated in Figure 16. With the increase in mesh size, the height difference of the workpiece surface in the measurement area decreases noticeably, and the number of peaks and troughs can be observed in the roughness profile. This is because as the mesh size increases, the particle size decreases, leading to a reduction in scratch depth on the workpiece surface. Additionally, with a decrease in mesh size, the number of abrasives increases, resulting in more scratches generated on the workpiece surface. This is reflected in the roughness profile, where the distance between adjacent peaks and troughs is significantly reduced, thereby enhancing the appearance of the workpiece surface to some extent.

The workpiece surface roughness value under different mesh sizes of the wheel is shown in Figure 17. It can be seen from the figure that the *Ra* of the workpiece surface decreases from 3.04 μm to 0.825 μm with an increase in wheel mesh size. The average relative deviations between the experimental and theoretical values for mesh sizes 80#, 160#, and 240# are 5.0%, 7.2%, and 8.6%, respectively. The *Ra* obtained by experiment follows the same variation rule as those obtained by numerical calculation. However, the calculated *Ra* is greater than that obtained from experimental measurements. This is because nanofluids were used as a cooling and lubrication medium during the experiment, which can improve the surface morphology of the workpiece to some extent. This condition was not considered in the calculation process.

4.3 Effect of Grinding Depth on Workpiece Morphology
4.3.1 Prediction Result
Under the condition where the wheel mesh is 80 and remains unchanged, the surface roughness is calculated

Table 3 High temperature nickel base alloy chemical composition

Element	C	Ni	Fe	Cu	Mn	Mo	Cr	Al	Co	Si
Ingredient/%	0.08	50–55	Remnant	0.3	0.35	2.8–3.3	17–21	0.95	1.0	0.35

Table 4 Mechanical properties of high temperature nickel-based alloys

Density (g/cm³)	Elastic modulus (GPa)	Thermal conductivity (W/m K)	Specific heat (J/ kg K)	Yield strength (MPa)	Tensile strength (MPa)	Poisson's ratio
8.24	199.9	14.7	435	550	965	0.3

Table 5 Physical properties of Al_2O_3 nanoparticles

Properties	Al_2O_3
Density (g/cm³)	0.35
Specific surface area (m²/g)	150
Particle size (nm)	50
Colour	White
Shape	Ball

Table 6 Experimental program

No.	Mesh	Cutting depth a_p (µm)	Feed speed v_w (m/min)	Wheel linear speed v_s (m/s)
1	80	10	2	30
2	80	20	2	30
3	80	30	2	30
4	160	20	2	30
5	240	20	2	30

by varying the grinding depth a_p, and the results are shown in Figure 18. When $a_p = 10$ µm, there may be gaps between the abrasives, resulting in areas of the workpiece that are not fully ground, and the furrows on the workpiece surface are shallow. As the grinding depth increases, more material is removed from the workpiece, resulting in an increase in the height difference of the workpiece surface profile.

The height matrix of a section on the workpiece surface is extracted perpendicular to the XOZ plane, and the roughness value of the workpiece at different grinding depths is then calculated. The corresponding relationship between different grinding depths and surface roughness is established by repeatedly calculating the surface roughness values using numerical analysis. As the grinding depth increases, the chip size increases, resulting in an increase in the height difference between the peaks and troughs of the workpiece surface profile. As the grinding depth increases from 10 µm to 30 µm, more material is removed by the abrasives, resulting in an increase in *Ra* from 2.63 µm to 3.87 µm.

4.3.2 Experimental Result

The surface morphology and roughness profile curves of the workpiece with grinding depths of 10 µm, 20 µm, and 30 µm under NMQL conditions were obtained using an 80# wheel, as shown in Figure 19. As shown in the figure, the height difference of the workpiece surface in the measurement area increases significantly with increasing grinding depth. This is because as the grinding depth increases, the grinding area of each abrasive and the maximum undeformed chip thickness increase. Consequently, the difference between the peaks and valleys on the surface roughness contour curve of the workpiece increases, leading to a deterioration in the surface morphology quality and an increase in surface roughness.

The experimental *Ra* value increases from 2.72 µm to 3.96 µm with the increase of grinding depth. For grinding depths of 10 µm, 20 µm, and 30 µm, the relative deviations between the experimental and numerical values are 3.4%, 8.4%, and 2.3%, respectively. Here, numerical analysis was performed on five sets of grinding depths, and experiments were conducted to verify three representative sets of grinding depths. Despite simplifying the experimental groups, the results still demonstrate the accuracy of the model and the consistency of the experimental patterns. The *Ra* obtained by experiment follows the same variation rule as that obtained by numerical calculation. However, the calculated *Ra* is smaller than that obtained from experimental measurements. From the analysis, it can be concluded that machine and wheel vibration during the experiment may reduce the surface morphology quality of the workpiece. This condition was not considered in the numerical analysis.
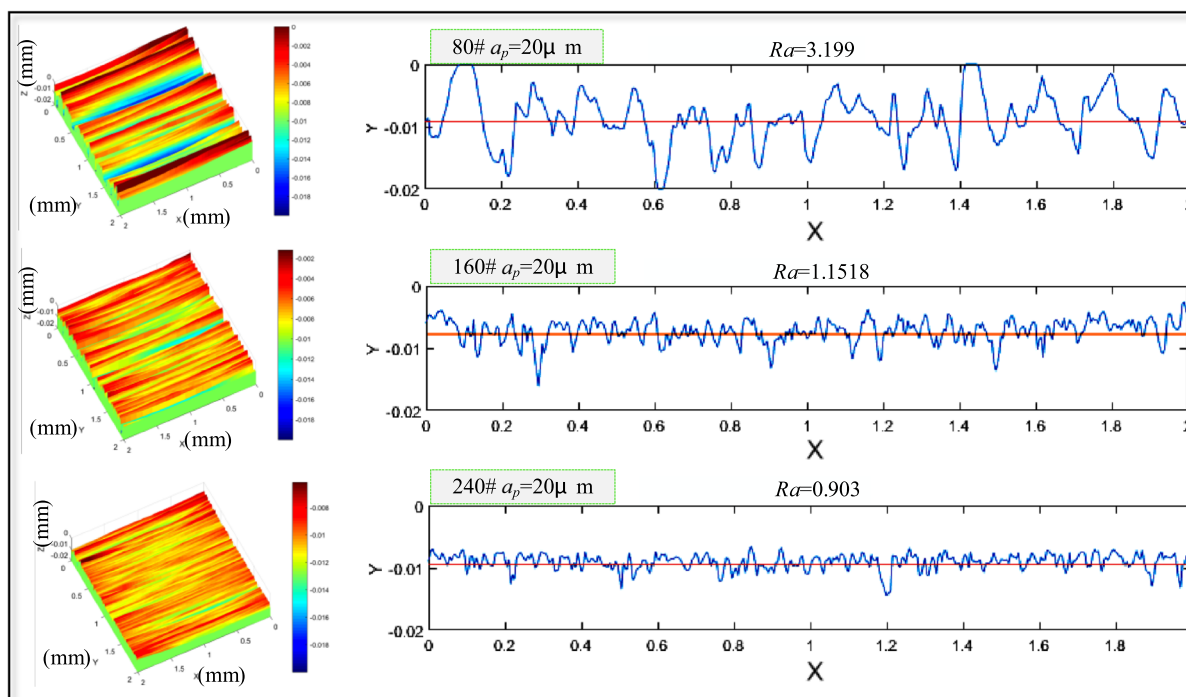
Zhang *et al. Chinese Journal of Mechanical Engineering*   (2024) 37:93

Page 16 of 23

Figure 15 Morphology and roughness profile curve of workpieces ground by grinding wheels with different meshes
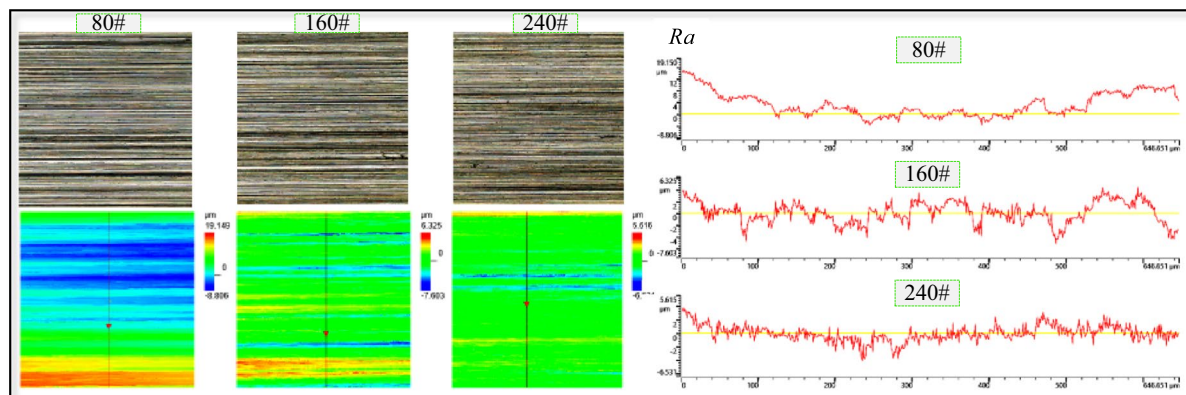

Figure16 Surface morphology and roughness profile curve of workpieces ground with different wheel meshes

4.4 The Fractal Dimension of the Workpiece Surface

The fractal theory analyzes the surface morphology of the workpiece based on its multi-scale, randomness, and self-affine properties resulting from grinding. Additionally, the *Ra* value of the workpiece varies significantly depending on the sampling area, evaluation length, and even the instrument used. The fractal dimension remains relatively stable regardless of changes in the sampling region under the same working conditions. The box dimension method calculates the 2D fractal dimension of the workpiece surface, as shown in Figure 20(a).

The box dimension is defined as covering the image with square boxes of size ε. Due to the characteristics of the image itself, the box can be divided into two states: with image and without image. The number of boxes with images is defined as $N(\varepsilon)$, and then by changing the size of ε, you can get a series of $N(\varepsilon)$ values. As ε approaches 0, $N(\varepsilon)$ also approaches infinity. By taking the logarithm
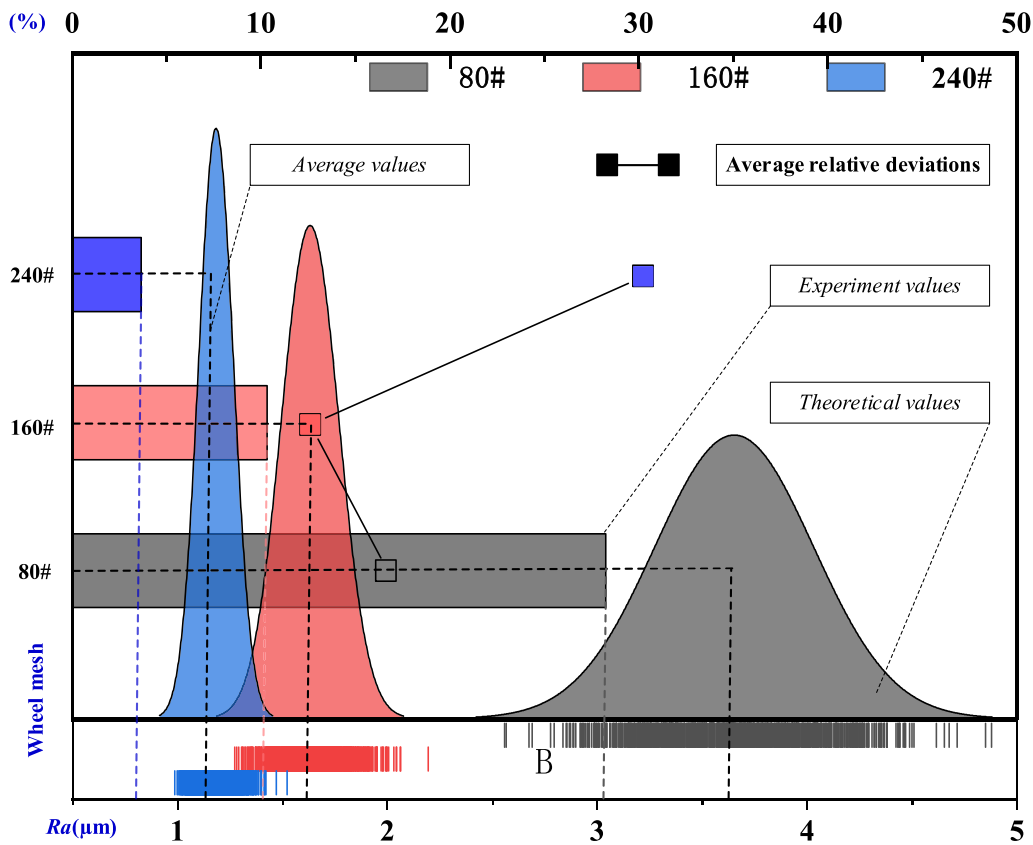
**Figure 17** Surface roughness values of workpieces under different wheel meshes

of ε and $N(\varepsilon)$, then using $\log_2 \varepsilon$ as the horizontal coordinate and $\log_2 N(\varepsilon)$ as the vertical coordinate, and fitting the data through the least square method, the negative value of the slope obtained is the box dimension, the formula is as follows:

$$D = -\lim_{\varepsilon \to 0} \frac{\log_2 N(\varepsilon)}{\log_2 \varepsilon}. \tag{40}$$

MATLAB is used to binarize the micrograph of the workpiece surface when calculating the box dimension of the workpiece surface. When the box covers all 0 matrices, it indicates that there is no relevant image region, while when the box covers non-0 matrices, it indicates that there is a relevant region in the box. With this method, we can calculate the number of $N(\varepsilon)$. The fractal dimension diagram of the workpiece surface with a 240# grinding wheel and a grinding depth of 20 μm after calculation and fitting by the box dimension method was shown in Figure 20(b). Under this condition, the fractal dimension of the workpiece surface is 1.87, the correlation coefficient is 1, and the maximum error is 2.8%. By calculating the fractal dimension of the workpiece surface

after machining with different wheel meshes and different grinding depths for many times and taking an average value, the relationship between the processing conditions and the fractal dimension was obtained.

When using an 80# mesh, the fractal dimension of the workpiece surface increases by 0.623% and 1.17% with a grinding depth of 10 μm compared to depths of 20 μm and 30 μm, respectively. Similarly, with a grinding depth of 20 μm, the fractal dimension of the workpiece surface after grinding with a 240# wheel increases by 0.692% and 1.19% compared to 160# and 80# wheels, respectively. Comparing the fractal dimension and Ra value and grinding depth when using an 80# wheel. At a grinding depth of 20 μm, the fractal dimension of the workpiece surface shows a negative correlation with Ra value and grinding depth. When the grinding depth is 20 μm, the fractal dimension of the workpiece surface is negatively correlated with Ra value and a positive correlation with the wheel mesh number. Smaller grinding depths result in larger fractal dimensions, whereas larger wheel meshes also result in larger fractal dimensions; however, the fractal dimension does not perfectly correlate with the Ra value.
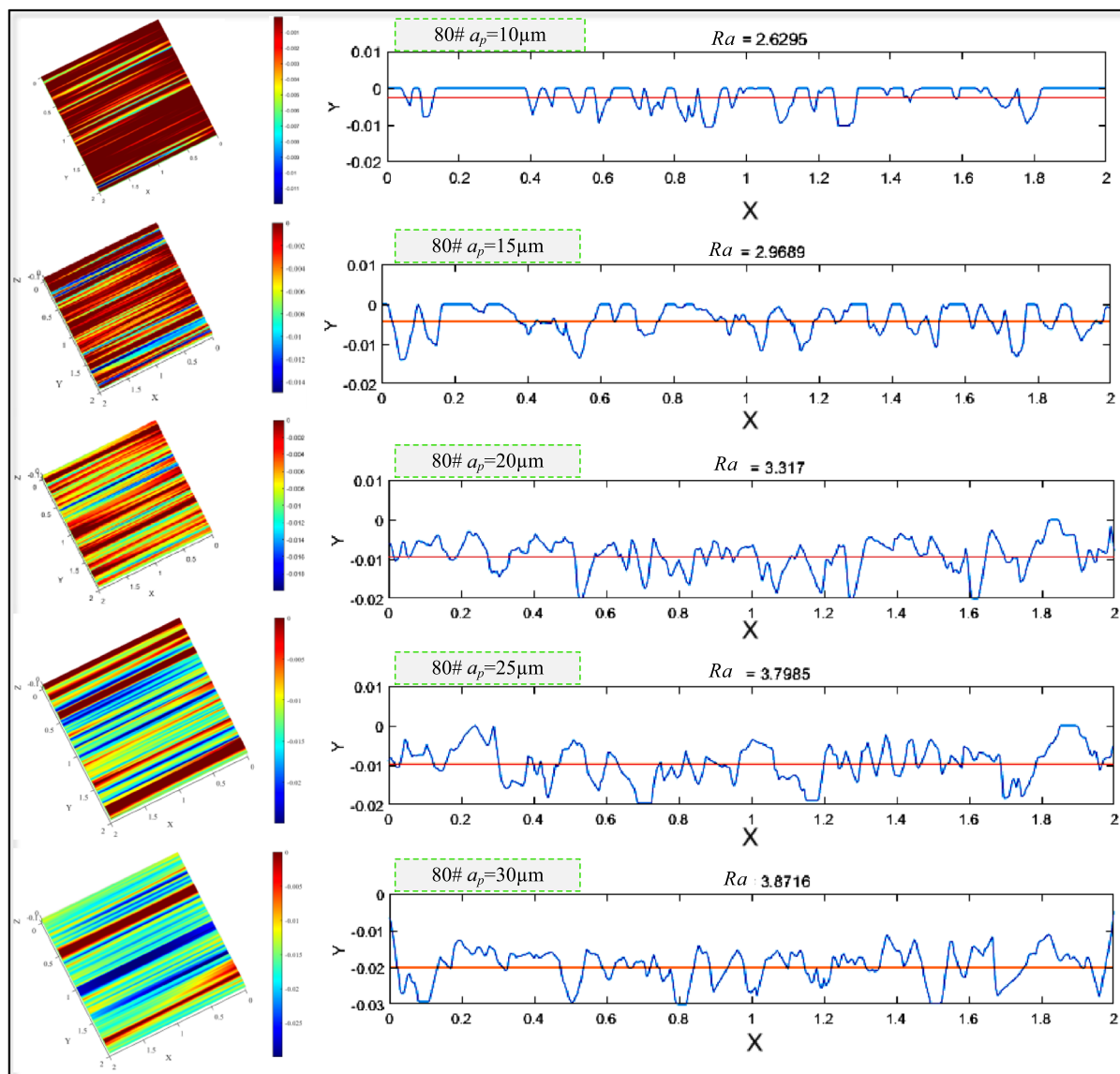
Figure 18 Surface morphology of workpieces with different grinding depths

5 Conclusions

To improve the surface morphology and roughness of workpieces during the grinding of high-temperature alloys and enhance the predictability of the process, this paper proposes a CBN wheel modeling and workpiece surface roughness prediction method based on the random plane method. And the effects of different parameters on the three-dimensional morphology and roughness of the workpiece surface are explored. The main research conclusions are as follows.

(1) A new method for geometric modeling of a single abrasive grain using the random plane method is proposed. Through fitting analysis, it is found that when the number of random planes is between 40 and 50, the calculated geometric shape of a single abrasive grain most closely resembles the actual abrasive grain. A kinematic model for a single abrasive grain is established, which accurately fits the three-dimensional morphology characteristics of the grinding wheel. The result shows that the height difference of the abrasive grains on the wheel surface is 300 μm.

(2) A workpiece surface elastic deformation and formation model based on Hertz theory is established, to reveal the variation of grinding arc length at differ-
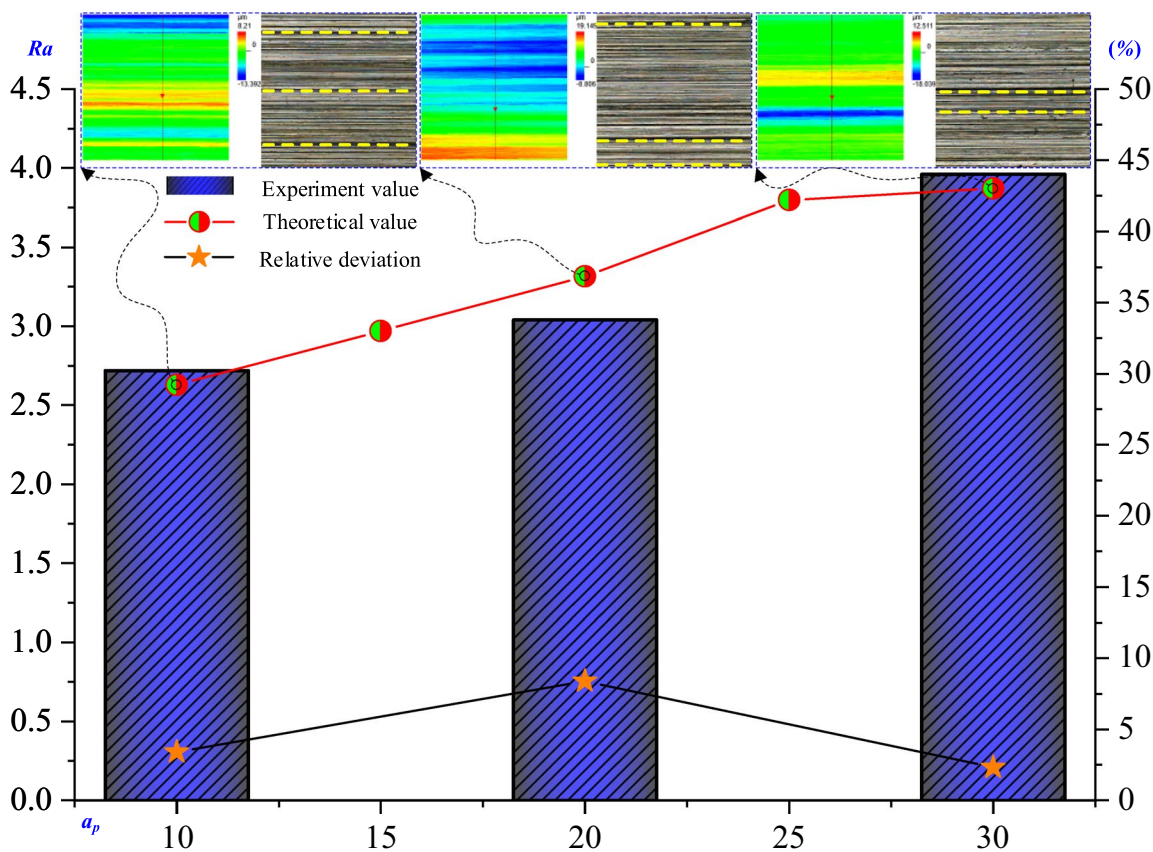
Figure 19 Surface morphology and roughness profile curves of workpieces at different grinding depths

ent grinding depths. The cycloid trajectory geometric characteristics of the workpiece surface formation are determined, and it is demonstrated that due to the elastic deformation of the grinding wheel and workpiece, as well as the influence of the random abrasive grain size, the grinding depth is less than the set depth.

(3) Based on the spatial distribution model of abrasive grains and the normal distribution model of grain size, geometric models of grinding wheels with different grit sizes and three-dimensional surface morphology models of the workpiece are established. The influence mechanism of the circumferential and axial distribution of abrasive grains on the surface formation of the workpiece is revealed. By combining the dynamic effective abrasive grain model with the influence of circumferential and axial abrasive grain distribution on the grinding trajectory of the workpiece surface, a predictive model for the surface morphology and roughness of the grinding wheel is established.

(4) Experiments are conducted to explore the influence of changing the grit size and grinding depth on the surface roughness of the workpiece, and verify the accuracy of the model. Results show that by varying the depth of grinding, model accuracy is in the range of 5.0 to 8.6 percent. By varying the grit size of the grinding wheel in the experiments, it is found that the actual three-dimensional morphology of the workpiece surface closely matches the model-predicted morphology, with the surface roughness prediction deviation as small as 2.3%.

Zhang *et al. Chinese Journal of Mechanical Engineering*　　(2024) 37:93

Page 20 of 23
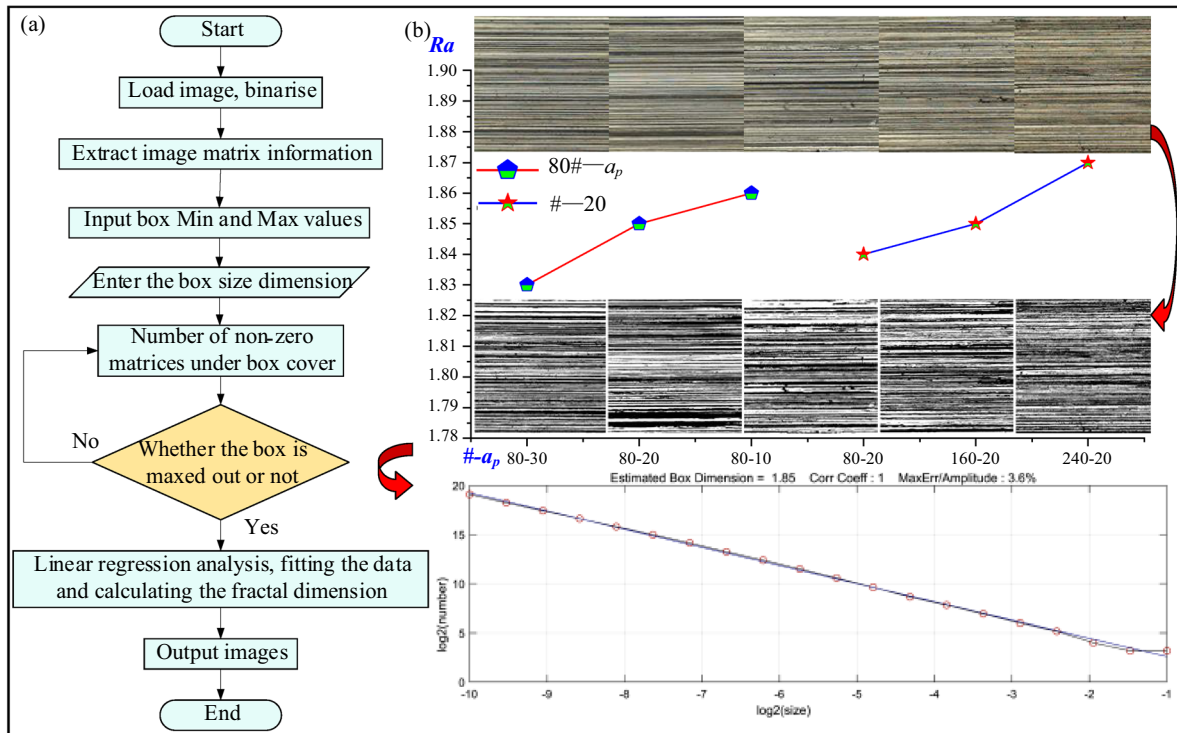
Figure 20 Fractal dimension calculation process and correlation coefficient of workpiece surface: (**a**) Calculation process of workpiece fractal dimension, (**b**) Measurement and fitting graph of fractal dimension

Data availability
This data is available for comparison of experimental and numerical analysis values, which can be seen in Fig. 19 Comparative Analysis.

Declarations

Competing Interests
The authors declare no competing financial interests.

Ethics approval and consent to participate
We declare that the papers we submitted are my research work under the guidance of the instructor and research results we have obtained. We confirm that this article has not been published previously and is not being submitted for publication elsewhere. We have not considered elsewhere except Chinese Journal of Mechanical Engineering. We confirm that this article has had the full consent of all authors. If this article was accepted, we confirm that it will not be published elsewhere in the same form, in English or in any other language, without the written consent of the publisher. The authors declare that they participated in this paper willingly.

Author Details
[1]Key Lab of Industrial Fluid Energy Conservation and Pollution Control, Qingdao University of Technology, Ministry of Education, Qingdao 266520, China. [2]School of Materials Science and Engineering, Xi'an University of Technology, Xi'an 710048, China. [3]College of Mechanical Engineering and Automation, Liaoning University of Technology, Jinzhou 121001, China. [4]Mechanical Engineering Department, Ahmadu Bello University, Zaria 810106, Nigeria.

References
[1] T. Zhu, M. Cai, Y. Gong, et al. Research progress of eco-friendly grinding technology for aviation nickel-based superalloys. *The International Journal of Advanced Manufacturing Technology*, 2023, 126: 2863-2886. https://doi.org/10.1007/s00170-023-11336-x
[2] M. Ganesh, N. Arunkumar, N.a. Kumar, et al. Investigation of surface grinding on Inconel under distinct cooling conditions. *Materials and Manufacturing Processes*, 2023, 38: 1823-1836. https://doi.org/10.1080/10426914.2023.2217896
[3] X. Wang, W. Ding, B. Zhao, et al. A review on machining technology of aero-engine casings. *Journal of Advanced Manufacturing Science and Technology*, 2: 2022011-2022011. https://doi.org/10.51393/j.jamst.2022011
[4] M. Yang, H. Ma, J. Hao, et al. Droplet size distribution model of needle electrode electrostatic atomization and milling nickel-based alloy

performance evaluation. *Journal of Manufacturing Processes*, 2024, 119: 682-698. https://doi.org/10.1016/j.jmapro.2024.04.011

[5] W. Xu, C. Li, X. Cui, et al. Atomization mechanism and machinability evaluation with electrically charged nanolubricant grinding of GH4169. *Journal of Manufacturing Processes*, 2023, 106: 480-493. https://doi.org/10.1016/j.jmapro.2023.10.037

[6] X. Cui, C. Li, Y. Zhang, et al. Grindability of titanium alloy using cryogenic nanolubricant minimum quantity lubrication. *Journal of Manufacturing Processes*, 2022, 80: 273-286. https://doi.org/10.1016/j.jmapro.2022.06.003

[7] N. Qian, W. Ding, Y. Zhu. Comparative investigation on grindability of K4125 and Inconel718 nickel-based superalloys. *The International Journal of Advanced Manufacturing Technology*, 2018, 97: 1649-1661. https://doi.org/10.1007/s00170-018-1993-y

[8] F. Zhang, Y. Zhang, C.F. Cheung, et al. A low temperature nano-lubrication method for enhancing machinability in ultra-precision grinding of binderless tungsten carbide (WC). *CIRP Annals*, 2023, https://doi.org/10.1016/j.cirp.2023.04.075

[9] G. Zhang, X. Deng, D. Liu, et al. A nano-MQL grinding of single-crystal nickel-base superalloy using a textured grinding wheel. *The International Journal of Advanced Manufacturing Technology*, 2022, 121: 2787-2801. https://doi.org/10.1007/s00170-022-09431-6

[10] M. Chen, R. Peng, L. Zhao, et al. Effects of minimum quantity lubrication strategy with internal cooling tool on machining performance in turning of nickel-based superalloy GH4169. *The International Journal of Advanced Manufacturing Technology*, 2022, 1-17. https://doi.org/10.1007/s00170-021-08194-w

[11] W. Ding, J. Xu, Z. Chen, et al. Grindability and surface integrity of cast nickel-based superalloy in creep feed grinding with brazed CBN abrasive wheels. *Chinese Journal of Aeronautics*, 2010, 23: 501-510. https://doi.org/10.1016/S1000-9361(09)60247-8

[12] Y. Zhang, L. Wenyi, T. Lizhi, et al. Abrasive water jet tool passivation: from mechanism to application. *Journal of Advanced Manufacturing Science and Technology*, 2022, 3: 2022018-2022018. https://doi.org/10.51393/j.jamst.2022018

[13] Y.X. Song, C.H. Li, Z.M. Zhou, et al. Nanobiolubricant grinding: a comprehensive review. *Advances in Manufacturing*, 2024, https://doi.org/10.1007/s40436-023-00477-7

[14] G. Xiao, J. Xing, Y. Zhang. Surface roughness prediction model of GH4169 superalloy abrasive belt grinding based on multilayer perceptron (MLP). *Procedia Manufacturing*, 2021, 54: 269-273. https://doi.org/10.1016/j.promfg.2021.07.042

[15] X. Xu, Y. Yu, H. Xu. Effect of grinding temperatures on the surface integrity of a nickel-based superalloy. *Journal of materials processing technology*, 2002, 129: 359-363. https://doi.org/10.1016/s0924-0136(02)00656-8

[16] H. Ji, Q. Song, M. Kumar Gupta, et al. Grain scale modelling and parameter calibration methods in crystal plasticity finite element researches: A short review. *Journal of Advanced Manufacturing Science and Technology*, 2021, 1: 41-50. https://doi.org/10.51393/j.jamst.2021005

[17] Z. Duan, S. Wang, Z. Wang, et al. Tool wear mechanisms in cold plasma and nano-lubricant multi-energy field coupled micro-milling of Al-Li alloy. *Tribology International*, 2024, 192: 109337. https://doi.org/10.1016/j.triboint.2024.109337

[18] Y. Zhou, X. Wen, G. Yin, et al. Study on theoretical model of roughness and wear of the microgrinding tool in microgrinding nickel-based single crystal superalloy. *Journal of the Brazilian Society of Mechanical Sciences and Engineering*, 2021, 43: 317. https://doi.org/10.1007/s40430-021-03034-0

[19] S.H. Chen, C.A. Yu. Prediction of tool lifetime and surface roughness for nickel-based waspaloy. *Advances in Materials Science and Engineering*, 2020, 2020: 12. https://doi.org/10.1155/2020/2013487

[20] H. Chen, J. Zhao, Z. Wang, et al. Modeling virtual abrasive grain based on random ellipsoid tangent plane. *The International Journal of Advanced Manufacturing Technology*, 2021, 113: 2049-2064. https://doi.org/10.1007/s00170-021-06742-y

[21] T.W. Liao. Fractal and DDS characterization of diamond wheel profiles. *Journal of materials processing technology*, 1995, 53: 567-581. https://doi.org/10.1016/0924-0136(94)01742-J

[22] J. Zhang, P. Guan, C. Su, et al. Simulation of grinding wheel with random three-dimensional abrasive and microporous bond. *Key Engineering Materials*, 2011, 487: 209-214. https://doi.org/10.4028/www.scientific.net/KEM.487.209

[23] Y. Liu, X. Huang, H. Cao, et al. Model of surface texture for honed gear considering motion path and geometrical shape of abrasive particle. *Chinese Journal of Mechanical Engineering*, 2023, 36: 96. https://doi.org/10.1186/s10033-023-00910-9

[24] M. Li, S. Zhao, H. Li, et al. On energy assessment of Titanium alloys belt grinding involving abrasive wear effects. *Chinese Journal of Mechanical Engineering*, 2023, 36: 115. https://doi.org/10.1186/s10033-023-00941-2

[25] Y. Liu, A. Warkentin, R. Bauer, et al. Investigation of different grain shapes and dressing to predict surface roughness in grinding using kinematic simulations. *Precision Engineering*, 2013, 37: 758-764. https://doi.org/10.1016/j.precisioneng.2013.02.009

[26] Y. Zhang, N. Xu, Y. Bao, et al. Surface topography and roughness prediction of axial ultrasonic assisted facing grinding metal. *Journal of Mechanical Engineering*, 2023, 59: 307-316. https://doi.org/10.3901/JME.2023.05.307

[27] H. Dong, H. Yang, X. Sun, et al. Surface roughness prediction of screw belt grinding based on improved neural network algorithm. *Surface Technology*, 2022, 51: 275-283. https://doi.org/10.16490/j.cnki.issn.1001-3660.2022.04.028

[28] L. Mingzheng, L. Changhe, Y. Zhang, et al. Analysis of grinding mechanics and improved grinding force model based on randomized grain geometric characteristics. *Chinese Journal of Aeronautics*, 2023, 36: 160-193. https://doi.org/10.1016/j.cja.2022.11.005

[29] R. Yan, Y. Rong, F. Jiang. Quantitive evaluation and modeling of alumina grinding wheel surface topography. *Journal of Mechanical Engineering*, 2011, 47: 179-186. https://doi.org/10.3901/jme.2011.17.179

[30] E.E. Hegeman, P.S. Levin. Using human health disparities and salmon health to guide spatial prioritization of green stormwater infrastructure. *Landscape and Urban Planning*, 2023, 240: 104905. https://doi.org/10.1016/j.landurbplan.2023.104905

[31] Y. Xiao, S. Wang, C. Ma, et al. Numerical modeling of material removal mechanism and surface topography for gear profile grinding. *Journal of Manufacturing Processes*, 2022, 76: 719-739. https://doi.org/10.1016/j.jmapro.2022.02.052

[32] Y. Zhang, X. Xu. Influence of surface topography evolution of grinding wheel on the optimal material removal rate in grinding process of cemented carbide. *International Journal of Refractory Metals and Hard Materials*, 2019, 80: 130-143. https://doi.org/10.1016/j.ijrmhm.2019.01.009

[33] S.J. Eder, U. Cihak-Bayr, A. Vernes, et al. Evolution of topography and material removal during nanoscale grinding. *Journal of Physics D: Applied Physics*, 2015, 48: 465308. https://doi.org/10.1088/0022-3727/48/46/465308

[34] M.X. Kang, D.Z. Hua, Y.B. Li, et al. Surface topography prediction of slider races using formed grinding wheel shape and material removal mechanism. *Archives of Civil and Mechanical Engineering*, 2024, 24: https://doi.org/10.1007/s43452-024-00939-0

[35] J. Wu, J. Cheng, C. Gao, et al. Research on predicting model of surface roughness in small-scale grinding of brittle materials considering grinding tool topography. *International Journal of Mechanical Sciences*, 2020, 166: 105263. https://doi.org/10.1016/j.ijmecsci.2019.105263

[36] Z.B. Hou, R. Komanduri. On the mechanics of the grinding process—Part I. Stochastic nature of the grinding process. *International Journal of Machine Tools and Manufacture*, 2003, 43: 1579-1593. https://doi.org/10.1016/S0890-6955(03)00186-X

[37] Q. An, J. Yang, J. Li, et al. A state-of-the-art review on the intelligent tool holders in machining. *Intelligent and Sustainable Manufacturing*, 2024, 1: 10002. https://doi.org/10.35534/ism.2024.10002

[38] X. Chen, W.B. Rowe. Analysis and simulation of the grinding process. Part II: Mechanics of grinding. *International Journal of Machine Tools and Manufacture*, 1996, 36: 883-896. https://doi.org/10.1016/j.ijmachtools.2003.09.008

[39] X. Chen, W.B. Rowe. Analysis and simulation of the grinding process. Part I: generation of the grinding wheel surface. *International Journal of Machine Tools and Manufacture*, 1996, 36: 871-882. https://doi.org/10.1016/j.ijmachtools.2003.09.008

[40] X. Chen, W.B. Rowe, B. Mills, et al. Analysis and simulation of the grinding process. Part III: Comparison with experiment. *International journal of machine tools and Manufacture*, 1996, 36: 897-906. https://doi.org/10.1016/j.ijmachtools.2003.09.008

[41] Z. Yin, J. Cheng, C. Dai, et al. Generation mechanism of the surface morphology on tilted ultrasonic elliptical vibration cutting TC4 titanium alloy.

Precision Engineering, 2024, 88: 135-147. https://doi.org/10.1016/j.precisioneng.2024.01.018

[42] X. Zhang. 3D simulation of surface-contact grinding tool topography. *Mechanical Engineer*, 2012, 16-17. https://doi.org/10.1007/s00170-012-4452-1

[43] L. Feng, G. Liu, Z. Li, et al. Study on the effects of abrasive particle shape on the cutting performance of Ti-6Al-4V materials based on the SPH method. *The International Journal of Advanced Manufacturing Technology*, 2019, 101: 3167-3182. https://doi.org/10.1007/s00170-018-3119-y

[44] Y.H. Sun, C.Y. Wang, Z. Qin. Modeling and simulation of abrasive belt grinding. *The 9th International Symposium on Advances in Abrasive Technology*, Dalian, Liaoning, China, 2006: 7.

[45] C.W. Dai, T.Y. Yu, W.F. Ding, et al. Single diamond grain cutting-edges morphology effect on grinding mechanism of Inconel 718. *Precision Engineering-Journal of the International Societies for Precision Engineering and Nanotechnology*, 2019, 55: 119-126. https://doi.org/10.1016/j.precisioneng.2018.08.017

[46] L. Benkai, D. Chenwei, D. Wenfeng, et al. Prediction on grinding force during grinding powder metallurgy nickel-based superalloy FGH96 with electroplated CBN abrasive wheel. *Chinese Journal of Aeronautics*, 2021, 34: 65-74. https://doi.org/10.1016/j.cja.2020.05.002

[47] Y. Zhou, Y. Gong, Z. Zhu, et al. Modelling and optimisation of surface roughness from microgrinding of nickel-based single crystal superalloy using the response surface methodology and genetic algorithm. *The International Journal of Advanced Manufacturing Technology*, 2016, 85: 2607-2622. https://doi.org/10.1007/s00170-015-8121-z

[48] X. Liang, Z. Liu, B. Wang, et al. Progressive mapping surface integrity and multi-objective optimizing surface quality of machining Ti-6Al-4V based novel tool failure criterion. *CIRP Journal of Manufacturing Science and Technology*, 2023, 42: 81-94. https://doi.org/10.1016/j.cirpj.2023.01.013

[49] T. Nguyen, J. Wang. A review on the erosion mechanisms in abrasive waterjet micromachining of brittle materials. *International Journal of Extreme Manufacturing*, 2019, 1: 012006. https://doi.org/10.1088/2631-7990/ab1028

[50] C. Li, Y. Hu, Z. Wei, et al. Damage evolution and removal behaviors of GaN crystals involved in double-grits grinding. *International Journal of Extreme Manufacturing*, 2024, 6: 025103. https://doi.org/10.1088/2631-7990/ad207f

[51] Q. Miao, W. Ding, T. Chen, et al. Surface gradient structures in single-crystal nickel alloy induced by ultrasonic-assisted high-speed grinding. *Materials Today Communications*, 2024, 38: 107930. https://doi.org/10.1016/j.mtcomm.2023.107930

[52] P. Gong, Y. Zhang, X. Cui, et al. Lubricant transportation mechanism and wear resistance of different arrangement textured turning tools. *Tribology International*, 2024, 109704. https://doi.org/10.1016/j.triboint.2024.109704

[53] L. Li, Y. Zhang, X. Cui, et al. Mechanical behavior and modeling of grinding force: A comparative analysis. *Journal of Manufacturing Processes*, 2023, 102: 921-954. https://doi.org/10.1016/j.jmapro.2023.07.074

[54] Y. Zhang. Grinding mechanism, forceprediction model and experimental validation of vegetable oil based nanofluids minimum quantity lubrication. 2018.

[55] X. Cui, C. Li, M. Yang, et al. Enhanced grindability and mechanism in the magnetic traction nanolubricant grinding of Ti-6Al-4V. *Tribology International*, 2023, 186: 108603. https://doi.org/10.1016/j.triboint.2023.108603

[56] L. Chen, Z. Liu, X. Wang, et al. Effects of surface roughness parameters on tribological performance for micro-textured eutectic aluminum–silicon alloy. *Journal of Tribology*, 2019, 142: https://doi.org/10.1115/1.4044990

[57] T. Zhang, C. Wu, C. Chen, et al. 3D bevel surface topography analysis and roughness prediction by considering the cutter-workpiece dynamic interaction. *The International Journal of Advanced Manufacturing Technology*, 2023, 129: 335-352. https://doi.org/10.1007/s00170-023-12265-5

[58] P. Gong, Y. Zhang, C. Wang, et al. Residual stress generation in grinding: Mechanism and modeling. *Journal of Materials Processing Technology*, 2024, 324: 118262. https://doi.org/10.1016/j.jmatprotec.2023.118262

[59] Z. Yang, L. Zhu, C. Ni, et al. Investigation of surface topography formation mechanism based on abrasive-workpiece contact rate model in tangential ultrasonic vibration-assisted CBN grinding of ZrO2 ceramics. *International Journal of Mechanical Sciences*, 2019, 155: 66-82. https://doi.org/10.1016/j.ijmecsci.2019.02.031

[60] W. Zhou, J. Tang, H. He, et al. Position-dependent rough surface formation in face gear worm grinding. *International Journal of Mechanical Sciences*, 2024, 270: 109076. https://doi.org/10.1016/j.ijmecsci.2024.109076

[61] Y. Zhang, T. Wu, C. Li, et al. Numerical simulations of grinding force and surface morphology during precision grinding of leucite glass ceramics. *International Journal of Mechanical Sciences*, 2022, 231: 107562. https://doi.org/10.1016/j.ijmecsci.2022.107562

[62] G. Xiao, Y. Zhang, B. Zhu, et al. Wear behavior of alumina abrasive belt and its effect on surface integrity of titanium alloy during conventional and creep-feed grinding. *Wear*, 2023, 514-515: 204581. https://doi.org/10.1016/j.wear.2022.204581

[63] K. Zhou, G. Xiao, J. Xu, et al. Wear evolution of electroplated diamond abrasive belt and corresponding surface integrity of Inconel 718 during grinding. *Tribology International*, 2023, 177: 107972. https://doi.org/10.1016/j.triboint.2022.107972

[64] K. Zhou, J. Xu, G. Xiao, et al. Enhancing ductile removal of Cf/SiC composites during abrasive belt grinding using low-hardness rubber contact wheels. *Ceramics International*, 2022, 48: 26042-26054. https://doi.org/10.1016/j.ceramint.2022.05.286

[65] Q. Cheng, C. Dai, Q. Miao, et al. Undeformed chip thickness with composite ultrasonic vibration-assisted face grinding of silicon carbide: Modeling, computation and analysis. *Precision Engineering*, 2024, 86: 48-65. https://doi.org/10.1016/j.precisioneng.2023.11.005

[66] Q. Miao, M. Lu, W. Ding, et al. Creep-feed grinding of single crystal nickel-base turbine blade fir-tree roots: tool wear, grinding force, temperature, and surface integrity. *The International Journal of Advanced Manufacturing Technology*, 2023, 126: 1453-1470. https://doi.org/10.1007/s00170-023-11188-5

[67] Q. Yin, C. Li, L. Dong, et al. Effects of physicochemical properties of different base oils on friction coefficient and surface roughness in MQL milling AISI 1045. *International Journal of Precision Engineering and Manufacturing-Green Technology*, 2021, 1-19. https://doi.org/10.1007/s40684-021-00318-7

[68] X. Cui, C. Li, Y. Zhang, et al. Tribological properties under the grinding wheel and workpiece interface by using graphene nanofluid lubricant. *The International Journal of Advanced Manufacturing Technology*, 2019, 104: 3943-3958. https://doi.org/10.1007/s00170-019-04129-8

[69] W. Guo, C. Wu, Z. Ding, et al. Prediction of surface roughness based on a hybrid feature selection method and long short-term memory network in grinding. *The International Journal of Advanced Manufacturing Technology*, 2021, 112: 2853-2871. https://doi.org/10.1007/s00170-020-06523-z

Yanbin Zhang   born in 1990, is currently a professor of *Qingdao University of Technology, China*. He received his PhD degree from *Qingdao University of Technology, China*, in 2018. His research interests include green grinding and precision machining, intelligent manufacturing and high-end equipment and intelligent agricultural machinery equipment.

Peng Gong   born in 1998, is currently a postgraduate of *Qingdao University of Technology, China*. His research interest is green precision machining.

Lizhi Tang   received his master's degree from *Qingdao University of Technology, China,* in 2022.

Xin Cui   born in 1990, is associate-professor of *Qingdao University of Technology, China*. She received his PhD degree from *Qingdao University of Technology, China*. Her current research interests focus on intelligent and clean precision grinding.

Dongzhou Jia   is associate-professor of *Liaoning University of Technology, China*. He received his PhD degree from *Qingdao University of Technology, China*. His current research interests focus on precision machining.

Zhang *et al. Chinese Journal of Mechanical Engineering*   (2024) 37:93

Page 23 of 23

Teng Gao born in 1993, is a PhD candidate of *Qingdao University of Technology, China*. His current research interests focus on intelligent and clean precision grinding.

Yusuf Suleiman Dambatta received his PhD degree from *University of Malaya, Malaya*. He is a senior lecturer at Ahmadu Bello University and Postdoctoral fellow at *Qingdao University of Technology, China*. His current research interests focus on Manufacturing systems and precision machining.

Changhe Li born in 1966, is a professor of *Qingdao University of Technology, China*. He is a special expert of Taishan Scholars in Shandong Province, China. He received his PhD degree from *Northeastern University, China*. His current research interests focus on intelligent and clean precision manufacturing. He has published 247 SCI/EI papers and won the China Patent Excellence Award (2 items) and Shandong Province Technical Invention 1st Prize.